# Confined molecular machines and switches

Danowski, Wojtek

*DOI:*
10.33612/diss.97039492

# Chapter 2
# Unidirectional Rotary Motion in a Metal Organic Framework

Overcrowded alkene-based light-driven molecular motors are able to perform large amplitude repetitive unidirectional rotations. Their behavior is well understood in solution; however, Brownian motion precludes the precise positioning at the nanoscale needed to harness cooperative action. Here we show molecular motors organized in crystalline metal organic frameworks (MOFs). The motor unit becomes a part of the organic linker (or strut) and its spatial arrangement is elucidated through powder and single crystal X-ray analyses, polarized optical and Raman microscopies. We confirm that the light-driven unidirectional rotation of the motor units is retained in the MOF framework and that the motors can operate in the solid state with similar rotary speed (rate of thermal helix inversion) to that in solution.

*This chapter was published as: Wojciech Danowski, Thomas van Leeuwen, Shaghayegh Abdolahzadeh, Diederik Roke, Wesley R. Browne, Sander J. Wezenberg, Ben L. Feringa, Nature Nanotechnology, 2019, 14, 488-494*

## 2.1 Introduction

Drawing inspiration from nature, the field of synthetic molecular machines has matured to the point that control of molecular motion can be successfully achieved in different molecular systems using external stimuli.[1–5] Virtually, all biological counterparts exhibit collective and cooperative behaviour requiring well-defined organization along multiple length scales.[6–8] To fully exploit the potential of artificial molecular machines and harness their collective motion it is crucial to incorporate them into nanostructured macroscopic materials allowing for precise spatial arrangement.[9–12]

The chiral overcrowded alkene based rotary molecular motors are unique in the sense that these molecules use light, heat, and stereochemical control to achieve unidirectional rotation.[13,14] The full 360° rotary cycle comprises two reversible photochemical *E*/*Z* isomerization steps, each followed by an irreversible thermally driven helix inversion in which the photogenerated metastable isomer converts to the stable isomer (Figure 1b), releasing steric strain. The overall unidirectionality of the rotary cycle is governed by the higher energy of the metastable compared to the stable isomer which renders the thermal helix inversion step energetically downhill. Previously, incorporation of these molecular motors into liquid crystals,[15–19] polymer gels,[20,21] muscle-like fibers,[22] as well as attachment to surfaces,[23,24] and 2-dimensional organization in the pores of tris(*o*-phenylene)cyclotriphosphazene (**TPP**)[25] has enabled, to some extent, cooperative action and macroscopic function. Nevertheless, attaining a perfect ordering in 3-dimensions in a solid-state material without impeding the motor function remains a fundamental challenge.[9,26]

Metal-organic frameworks (MOFs) constitute ideal platforms to spatially organize molecular motors in a precise and predictable manner.[9,10,26–28] MOFs are porous 3-dimensional materials consisting of inorganic nodes (metal ions or clusters), bridged by organic linkers and, due to their inherent porosity, typically possess large free volume, essential for the dynamic behaviour in the solid material.[29,30] Recent studies showed that linker rotors can undergo small amplitude non-directional rotations when embedded in a MOF framework,[31–35] while [2]rotaxane struts exhibited large amplitude pirouetting and shuttling motion when embedded in a MOF.[36–39] In a different investigation, electrochemical switching and large amplitude rotational motion of a redox-active bistable catenane, which was introduced in the MOF framework by solvent assisted linker incorporation (SALI), was demonstrated.[40] Nevertheless, towards efficient collective and cooperative behaviour and creation of the machine like function in nanostructured condensed phase, it remains challenging to avoid a decrease in the rate of molecular motion and to achieve a motion with directional bias.

Here we report the 3-dimensional organization of light-driven rotary molecular motors in the solid state using a MOF as a platform for achieving well-defined spatial organization. The desired motorized MOF (here denoted as moto-MOF**s** containing motor **1** or **2**-***E***/***Z*** as pillars, Figure 2.1) materials were prepared via a post-synthetic method, and possesses sufficient free volume (larger than the volume that the molecular motor occupies) to ensure uncompromised large amplitude unidirectional rotary motion of the linker-based motor in the solid state.

## 2.2 Synthesis

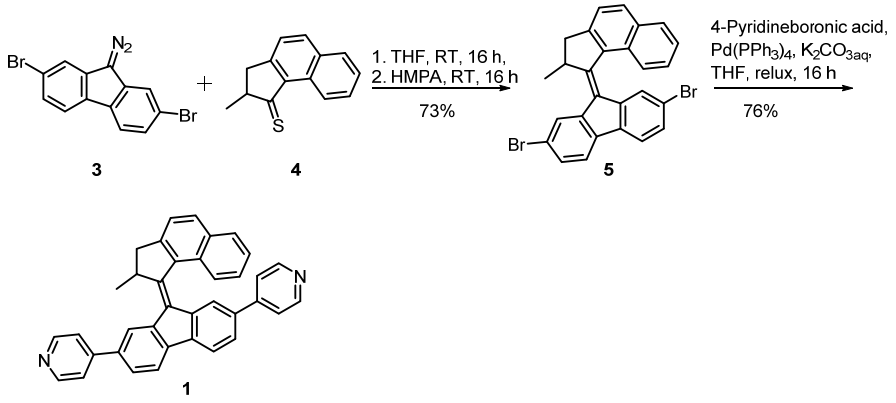


***Scheme 2.1*** *Synthesis of molecular motor pillar **1***

Molecular motor **1** was synthesized in two steps from known compounds. First, dibromo functionalized motor **5** was synthesized in a Barton-Kellog reaction from diazo **3** and thioketone **4**. Next, pyridyl functionalities were introduced with Suzuki cross-coupling with 4-pyridinylboronic acid to afford bispyridyl functionalized motor **1** in a good yield.

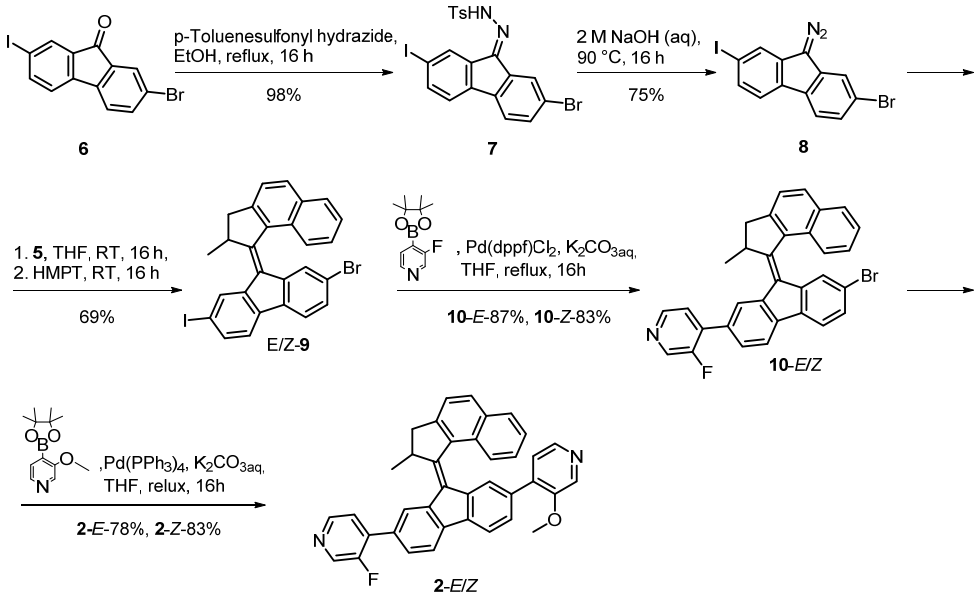


***Scheme 2.2*** *Synthesis of molecular motor pillars* ***2-E/Z***

Synthesis of the motors **2-*E*/*Z*** bearing desymmetrized lower half commenced with the synthesis of 2-bromo-7-iodofluorenone **6** according to the literature procedure.[41] Next, the fluorenone **6** was converted into the corresponding tosylhydrazone **7** in a condensation reaction with N-tosylhydrazide. Heating of the aqueous suspension of **7** with a base afforded, after crystallization from cold ether, diazo compound **8** as a stable, pink, crystalline solid. Diazofluorene **8** was subsequently used in the Barton-Kellog olefination with thion **5**, which afforded molecular motor **9** as an inseparable mixture of diastereoisomers. Subsequently, motor **9** was functionalized with 3-fluoropyridine in a Suzuki cross-coupling reaction and at this stage the diastereoisomers could be separated by column chromatography yielding **10-*E*** and **10-*Z***. Noteworthy, the reaction proceeded smoothly with $Pd(dppf)Cl_2$ catalyst, whereas the reaction with $Pd(PPh_3)_4$ catalyst led mostly to decomposition products. The resulting motors **10-*E*** and **10-*Z*** were further functionalized with 3-methoxypyridine to give the desired products **2-*E*** and **2-*Z***. The geometry of both isomers was assigned based on the $^1$H NMR shifts of the methoxy group, as in **2-*E*** the methoxy group is located in the vicinity of the shielding aromatic ring current of the upper-half (Scheme 2.3), which results in downfield shift of the resonance of the methoxy protons in comparison to **2-*Z*** (**2-*Z***: 4.00 ppm **2-*E***: 3.71 ppm).

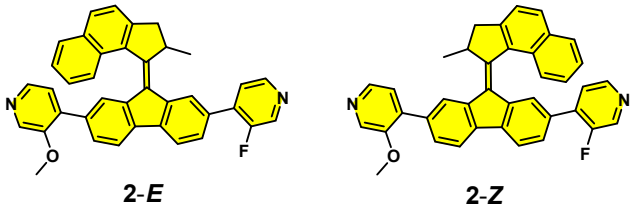


***Scheme 2.3*** *Structure of* ***2-E*** *and* ***2-Z***

## 2.3 Design, synthesis and characterization of the Motorized Metal Organic Frameworks

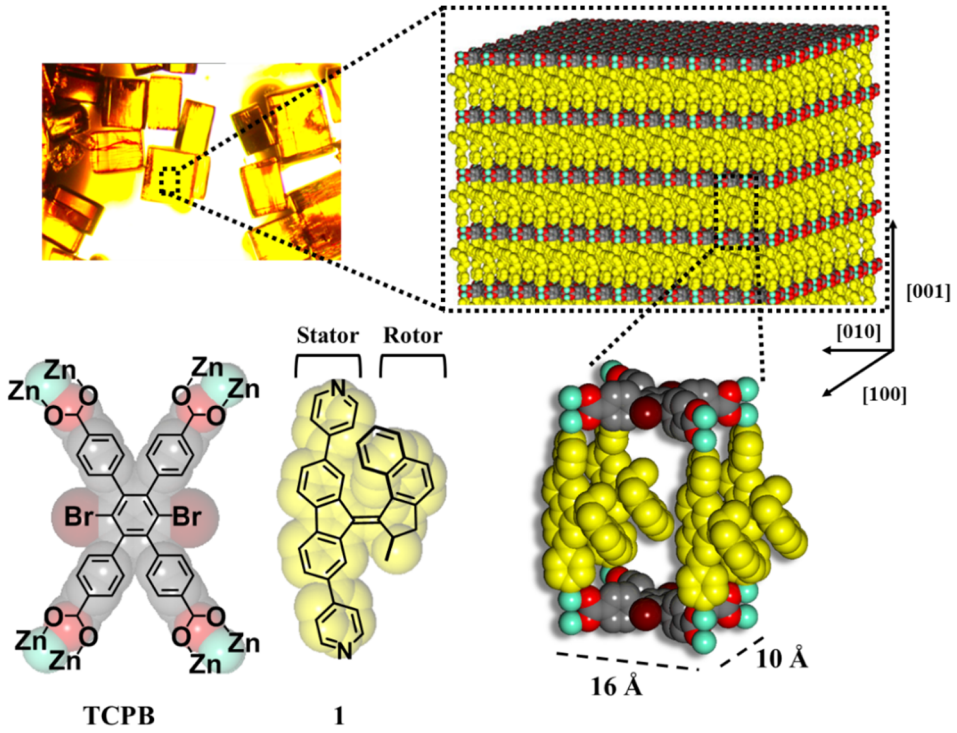


***Figure 2.1*** *Schematic representation of the 3-dimensional organization of molecular motor* ***1*** *in moto-MOF representing packing in the crystal, elementary cell, and structure of the linkers: tetracarboxylic acid (****TCPB****) and molecular motor (****1****) used to construct the framework. In the designed framework, the stator of the motor (i.e. lower-half) is used to bridge the 2-D layers constructed from Zn paddlewheel clusters and* ***TCPB****, while the rotor moiety (i.e. upper-half) can rotate freely with respect to the lower-half*

Taking into consideration the free volume required for proper motor functioning in the crystalline MOF, the material of choice was a zinc pillared-paddlewheel

BrYO-MOF.[42] This type of MOF consists of layers formed by zinc paddlewheel nodes, which are bridged by tetracarboxylic acids linkers (**TCPB**, Figure 2.1). The layers are connected in the third dimension by 4,4'-bipyridine-derived pillars, and the distance between the nodes is approximately 10 Å (in the [100] direction) and 16 Å (in the [010] direction). It was envisioned that incorporation of the dipyridyl-functionalized motor **1** (the rotor moiety is 8 Å in length) (Figure 2.1) within this framework should provide enough free space for unhindered rotation of the motor unit (The free volume in the parent MOF[42] was estimated as the solvent accessible volume which was mapped using a probe radius - 1.5 Å with grid spacing - 0.1 Å (Mercury Software) giving a free volume of 1470 $Å^3$ (39.4% of the cell volume), while the volume required for the unhindered rotation of motor was estimated to be 423 $Å^3$). Since the overcrowded olefinic bond of **1** might react under the relatively harsh conditions required for MOF synthesis,[43] we opted for a post-synthetic fabrication method of the material, i.e. a Solvent-Assisted Linker Exchange (SALE).[44] In this process, dipyridyl-naphthalenediimide pillars (**DPNI**) can be readily replaced with a broad range of bipyridines allowing for fabrication of new MOF materials under much milder conditions than used in *de novo* synthesis (Figure 2.2).

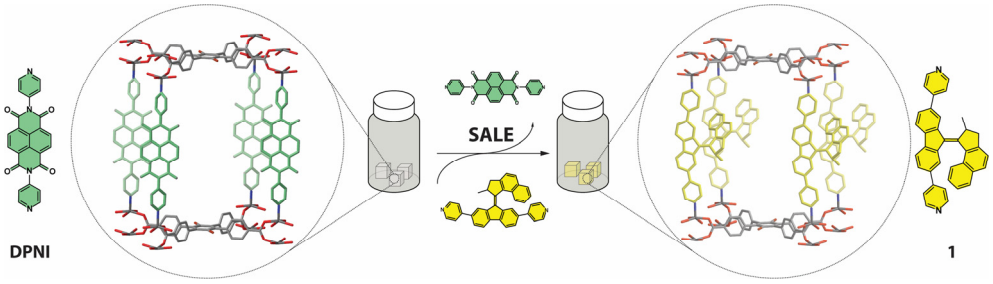


***Figure 2.2*** *Schematic representation of the synthesis of the MO-MOFs via SALE. Crystals of the parent framework were immersed in a solution of* ***1****,* ***2-E*** *or* ***2-Z*** *during which bipyridine motor* ***1****,* ***2-E*** *or* ***2-Z*** *(yellow) replaced the parent* ***DPNI*** *(green) pillars in the structure.*

Hence, a parent MOF constructed from 1,4-dibromo-2,3,5,6-tetrakis(4-carboxyphenyl)benzene (**TCPB**) and **DPNI** was employed.[42] Subsequently, SALE was carried out by immersing the colourless crystals of this parent MOF (Figure 2.3a) in a DMF solution containing **1** at 60 °C for 24 h, which afforded yellow crystals of moto-MOF**1** (Figure 2.3b). Moto-MOF**2-*E*** and moto-MOF**2-*Z*** were synthesized in a similar way, but the exchange was carried over four days and the solution was replaced with a fresh batch every 24 h to achieve full exchange (Figure 2.3c,d).

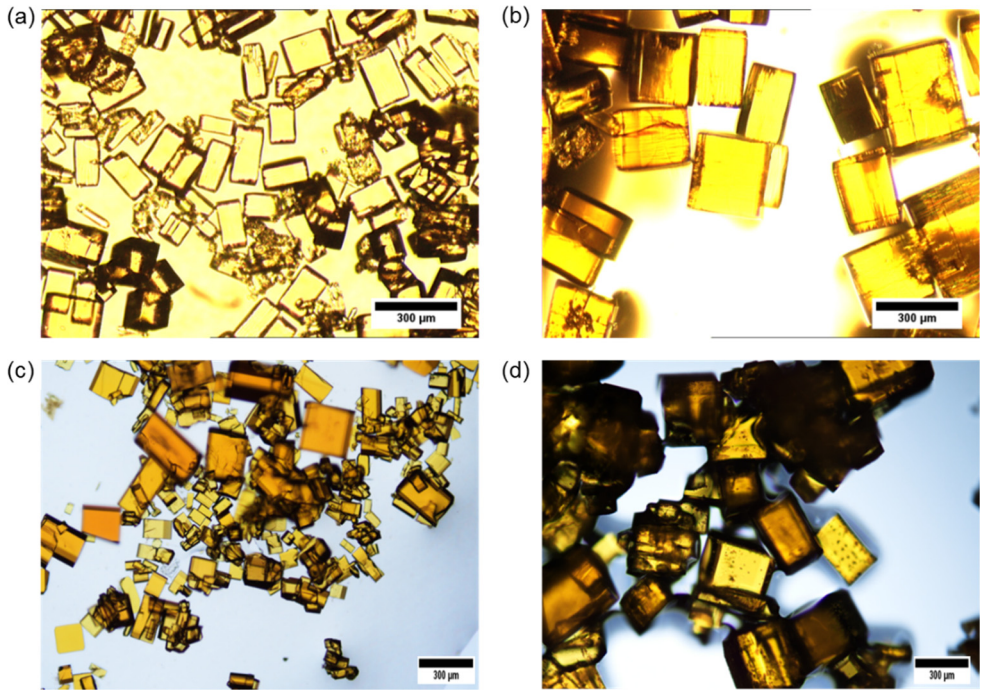


***Figure 2.3*** *Optical microscope images of* ***(a)*** *a parent MOF,* ***(b)*** *moto-MOF****1****,* ***(c)*** *moto-MOF****2-Z*** *and* ***(d)*** *moto-MOF****2-E*** *(scale bar 300 µm).*

Characterization by $^{1}$H NMR spectroscopy of digested (using $D_2SO_4$) crystals of moto-MOF**s** in $d_6$-DMSO showed the expected 1:1 ratio of **TCPB** and respective motor, supporting a successful exchange (Figure 2.4a). Bands characteristic of the overcrowded olefin and **TCPB** are observed by Raman spectroscopy, while bands characteristic of **DPNI** were not observed. (Figure 2.4b,c). The anticipated composition of the moto-MOF**1** was further confirmed by elemental analysis and Inductively Coupled Plasma Atomic-Emission Spectroscopy (ICP-AES), of which the analysis results corresponded well to the anticipated 1:1:2 ratio of **1**:**TCPB**:**Zn**.

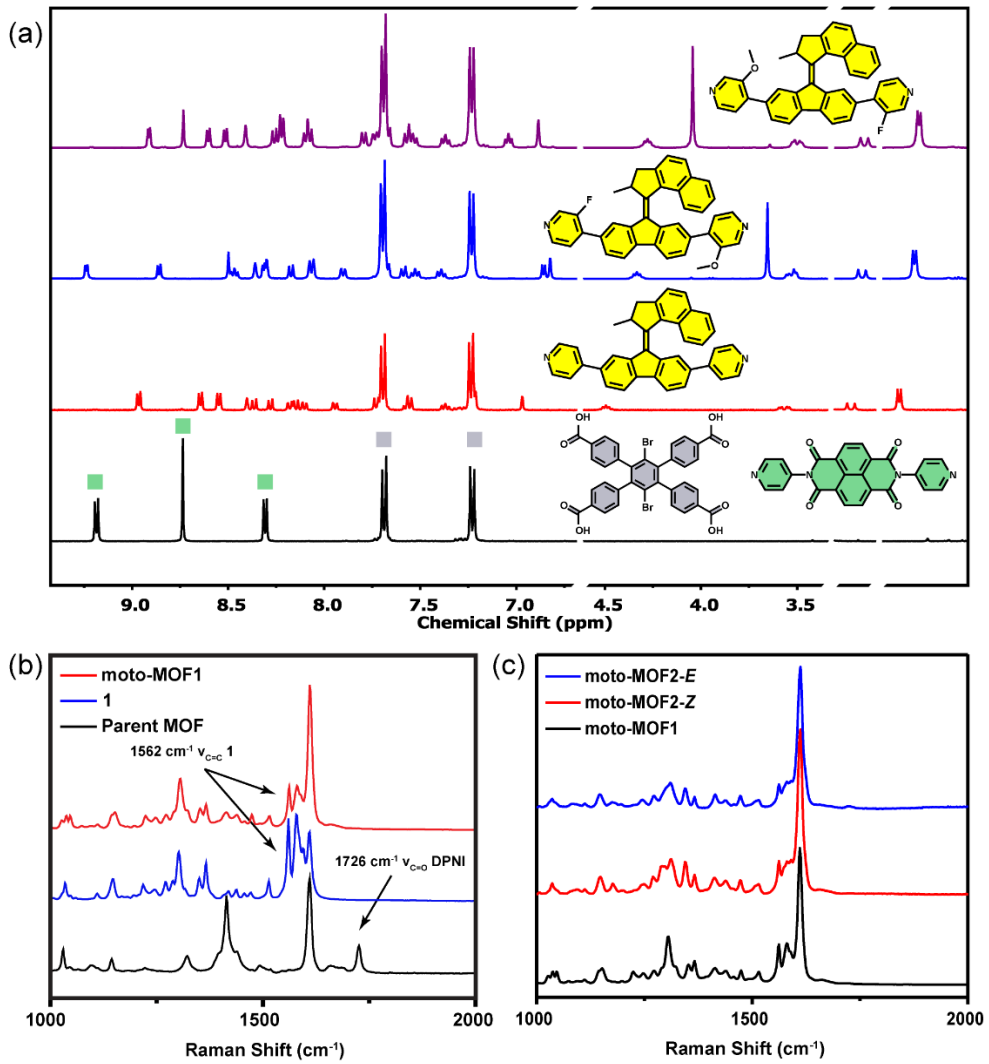


***Figure 2.4*** ***(a)*** *$^1$H NMR (400 MHz, $d_6$-DMSO) of digested (with $D_2SO_4$) crystals of parent MOF (black line), moto-MOF**1** (red line), moto-MOF**2-E** (blue line), moto-MOF**2-Z** (violet line). Coloured rectangles denote resonances of the aromatic protons of **TCPB** and **DPNI**.* ***(b)*** *Raman spectra (785 nm, 50 mW) of a parent MOF (black line) showing bands characteristic of both **DPNI** and **TCPB** (**DPNI** 1726 cm$^{-1}$ $\nu_{C=O}$, and **TCPB** 1610 cm$^{-1}$ $\nu_{C=C}$ of aromating rings). In the spectrum of moto-MOF**1** (red line) bands characteristic of **DPNI** are absent and bands consistent with **1** (blue line) are present ($\nu_{C=C}$ of the central double bond 1562 cm$^{-1}$).* ***(c)*** *Comparison of Raman spectra of moto-MOF**1** (black line), moto-MOF**2-Z** (red line) and moto-MOF**2-E** (blue line).*

Powder X-Ray Diffraction (PXRD) data, acquired under solvent saturated conditions, showed that the crystallinity of the material was preserved in all cases throughout the SALE process (Figure 2.5a,b). The PXRD pattern of the moto-MOFs is similar to the pattern observed for the parent material in terms of peak positions. However, slight differences in terms of the relative peak intensities were observed, assigned to the differences in electron density in the crystal structure originating from the substitution of the **DPNI** pillar in the framework. Nevertheless, the position of the first peak at 2θ = 4.00°, which corresponds to the reflection from the (001) plane, remains unchanged (Figure 2.5a,b inset). This observation is consistent with the fact that the **DPNI** linker and bipyridyl-functionalized molecular motor **1** have similar N-N distances (N-N distances in DFT optimized structures (B3LYP, 631-G(d,p) 15.6 Å **DPNI**, 15.4 Å **1**).

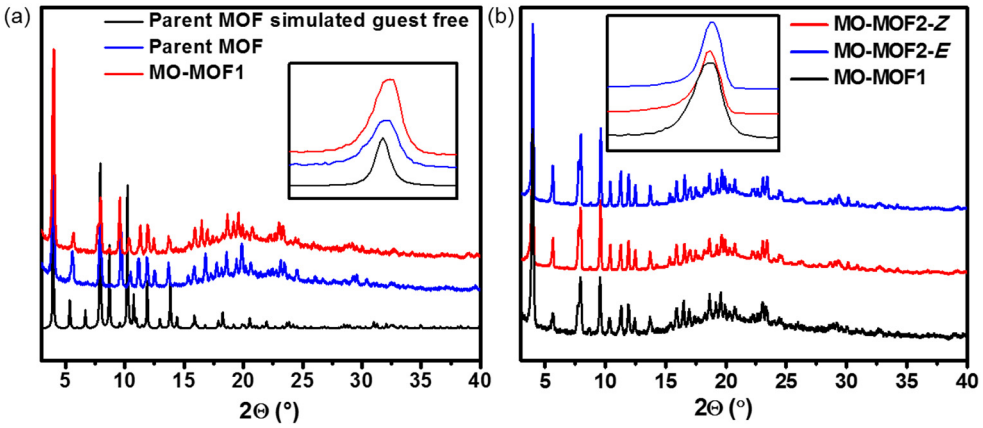


***Figure 2.5*** *(**a**) Comparison of the PXRD patterns of MOFs, simulated parent MOF (intensity of first peak was decreased three times, black line), experimental parent MOF (blue line), MO-MOF**1** (red line), inset shows expanded region around first peak. (**b**) Comparison of the PXRD patterns of MO-MOFs with motors **1** (MO-MOF**1**, black line),* **2-E** *(MO-MOF**2-E**, blue line), with motor **2-Z** (MO-MOF**2-Z**, blue line) pillars.*

The single crystal X-Ray diffraction data of MO-MOF**1** could only be partially resolved. From the solution of the diffraction data and initial refinement, the position of the Zn cations and the **TCPB** fragment were located, but for the molecular motor moieties (apart from the pyridyl nitrogen atoms) this was not possible due to a degree of disorder (Figure 2.6a,b). It can be calculated on the basis of the elementary cell dimensions (a 16.202 Å, b 10.742 Å, c 22.2582 Å), that one $cm^3$ of MO-MOF**1** contains approximately $4 \times 10^{20}$ motor units, illustrating that densely functionalized responsive materials can be created in this way.

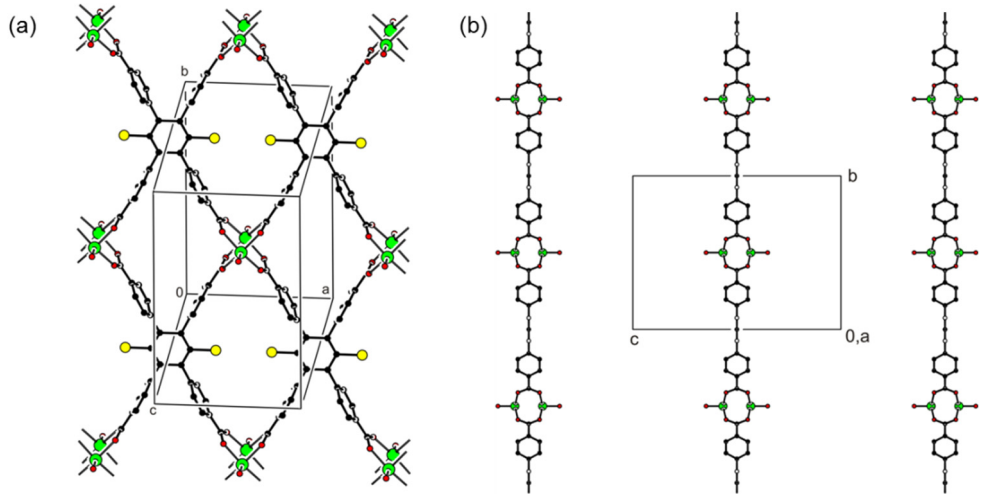


***Figure 2.6*** *(**a**) Packing diagram of the **TCPB** in the unit cell of the MO-MOF**1**. (**b**) Stacking of the two-dimensional layers in the* c *direction. Hydrogen atoms and disordered guest molecules have been omitted in the drawing. Zinc atoms are drawn in green, bromines in yellow, carbons in black, and oxygens, nitrogens in red. The volume between the layers is filled with diffuse electron density.*

Furthermore, Polarized Optical Microscopy (POM) showed that MO-MOF**1** crystals are birefringent indicating that the motor units are predominantly orientated in the same direction in the crystal (Figure 2.7a). In addition, the polarized Raman spectra of the MO-MOF**1** crystals showed significant variation of the polarizability of the bands characteristic of the C=C stretching with respect to the polarization axis of the laser, upon rotation of the crystal over 180° (15° steps). It was found that the band ascribed to the stretching of the overcrowded double bond of **1** exhibit one maximum. A similar trend was observed in the band due to the stretching of the double bonds in the aromatic rings of both **TCPB** and **1**. (Figure 2.7b). The disorder in the crystal thus most likely arises from the different orientations of the rotor units in **1** along the [001] direction.

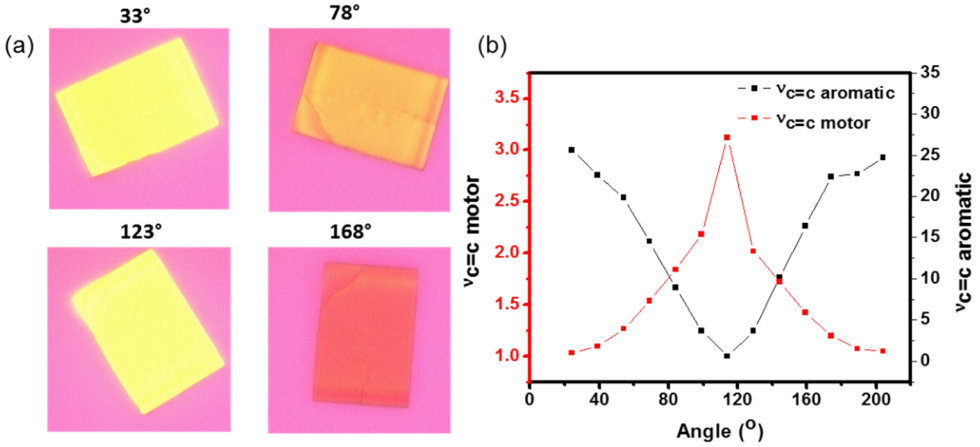


***Figure 2.7*** *(**a**) Polarized optical microscope (POM) images of the MO-MOF**1** crystals. The crystal was rotated by 33°, 78°, 123° and 168° with respect to the transmission axis of analyzer. (**b**) Angle dependence of the (normalized) ratio of the band areas recorded with a polarized and non-polarized laser, for the bands centered at 1562 $cm^{-1}$ (stretching of the central double bond of the molecular motor, red squares, left axis) and 1610 $cm^{-1}$ (C=C stretching in the aromatic rings of both **1** and **TCBB**, black rectangles, right axis). During the measurement, the sample was kept under solvent-saturated conditions in a closed quartz cuvette to avoid drying. The sample of the MO-MOF**1** was placed on the manual rotary table, mounted to the microscope stage. Raman spectra were taken in the direction perpendicular to the (001) plane of the single MO-MOF**1** crystal with the linearly polarized and non-polarized laser upon rotating the table every 15°.*

## 2.4 Photochemical and thermal isomerization in solution.

The rotary behaviour of molecular motor **1** was characterized in solution by UV/Vis absorption and NMR spectroscopies. Upon irradiation of **1** at 395 nm at -30 °C in $CDCl_3$, a new set of $^1H$ NMR resonances, indicative of the formation of the metastable isomer, appeared and a photostationary state (PSS) ratio of 83:17 (metastable:stable) was established. Warming the sample to room temperature resulted in full conversion of the metastable to the stable isomer (Figure 2.1).

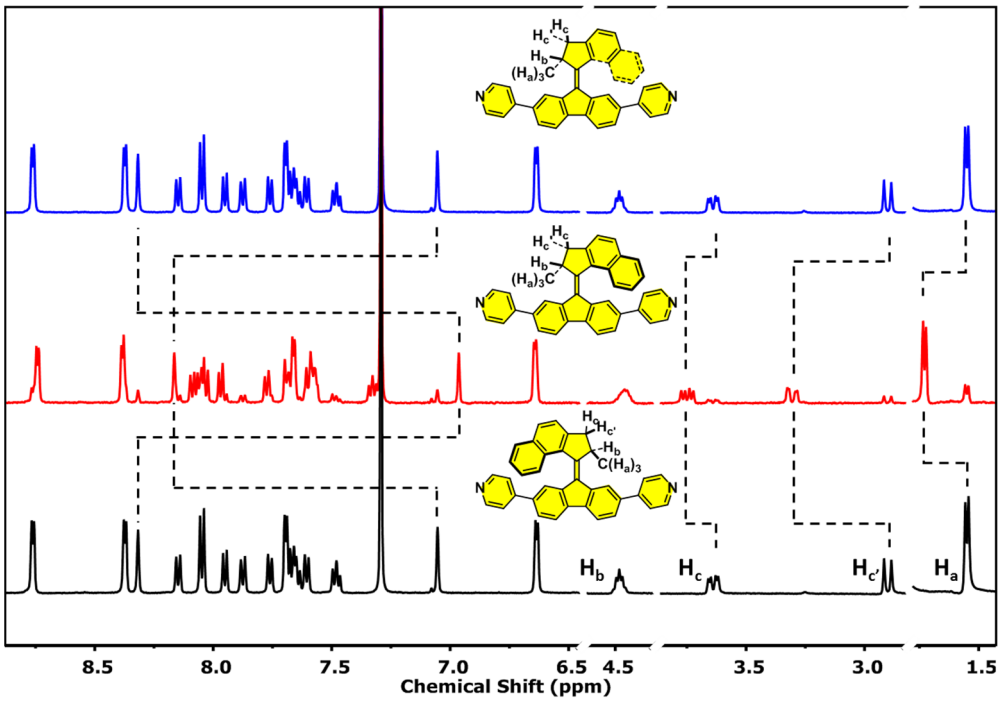


***Figure 2.8*** *Comparison of the $^{1}$H NMR (500 MHz, $CDCl_3$, -30 °C) spectra of stable* ***1*** *(black, bottom spectrum), PSS mixture (red, middle spectrum) and the PSS mixture kept in the dark at room temperature overnight (after THI, blue, top spectrum). A PSS ratio of 83:17 (metastable:stable) was determined by integration of the aliphatic signals of the metastable form and stable form.*

In the UV/Vis absorption spectrum, a gradual bathochromic shift of the main absorption band occurred with an isosbestic point maintained at 420 nm upon irradiation at 395 nm, consistent with the formation of the metastable isomer (Figure 2.9a). The rate of the thermal helix inversion (THI) was determined by following the exponential decrease of the main absorption band of the metastable isomer in the temperature range (7–16 °C) in $CHCl_3$, in DMF, and in heptane. Eyring analysis showed that the Gibbs energy of the activation for the thermal helix inversion is similar in all examined solvents (Figure 2.9b-d). The experimental values matched closely to the barrier for THI calculated by DFT methods at the B3LYP 6-31G(d,p) level of theory confirming the unidirectional rotation of the molecular motor **1** ($\Delta^{\ddagger}G_{calc}$(20 °C) = 90.3 kJ mol$^{-1}$, Table 1, Table 2).

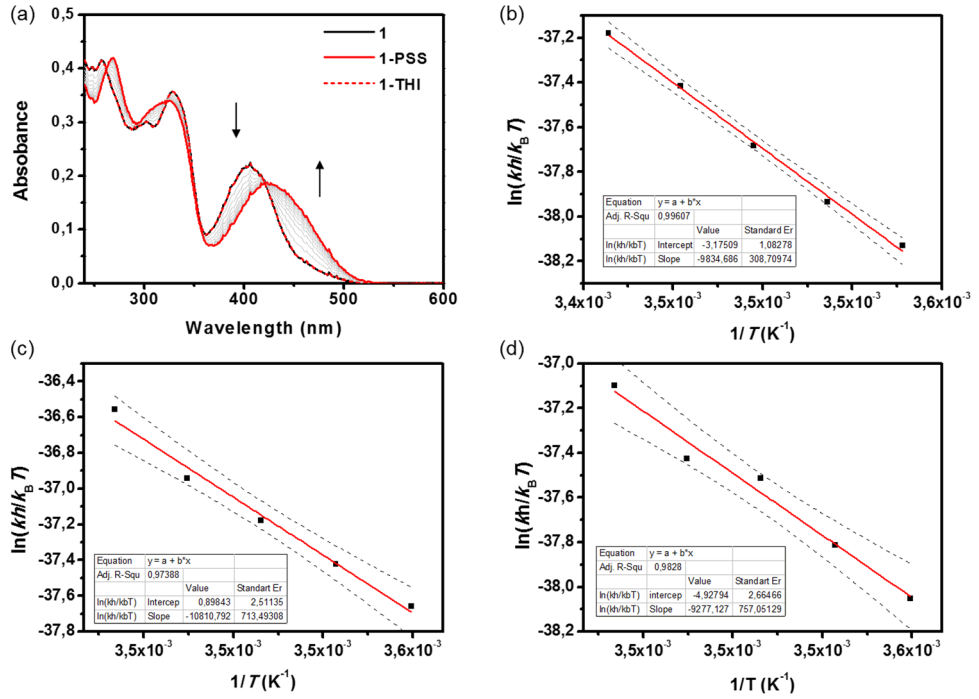


***Figure 2.9*** *(**a**) UV/Vis absorption spectrum of **1** before (black solid line) and after irradiation to the PSS (red line) at 395 nm (at 7 °C, $CHCl_3$) and after subsequent THI (red dashed line). An isosbestic point is maintained at 420 nm. Eyring plot analysis of thermal isomerization step from metastable **1** to stable **1** in (**b**) heptane, (**c**) DMF, (**d**) Chloroform. Thermodynamic parameters of the transition state were obtained by fitting the linearized form of the Eyring equation using Origin software. Dashed lines indicate 95% confidence intervals.*

***Table 1*** *Characteristics of rotary motor **1** in solution, in moto-MOF**1**, moto-MOF**2-Z** and calculated values*

| | $\Delta^{\ddagger}G$(20 °C) (kJ mol$^{-1}$) | $t_{1/2}$ (min) |
|---|---|---|
| Heptane | 89.5±0.2[a] | 17 |
| Chloroform | 89.1±0.7[a] (88.9±0.3[c]) | 15 |
| DMF | 87.7±0.6[a] | 8.0 |
| DMF $\mathbf{1H_2}^{2+}$ | 87.7±0.1[a] | 8.0 |
| Calculated | 90.3[b] | 23 |
| moto-MOF**1** | 88.6±0.7[c] | 12 |
| moto-MOF**2-*Z*** | 88.9±1.3[c] | 13 |

*[a]determined by UV/Vis spectroscopy based on Eyring analysis, [b]DFT B3LYP 6-31G(d,p), [c] derived from the rate constant determined by Raman spectroscopy at room temperature*

Additional studies were performed on bis-protonated **1**. UV/Vis absorption (conducted in DMF) and $^1$H NMR (conducted in $d_4$-MeOH) spectroscopies confirmed that protonation of **1** did not affect significantly the photochemical isomerization behaviour nor the barrier for thermal helix inversion (photostationary state ratio 68:32 metastable:stable, $\Delta^{\ddagger}G_{DMF}$(20 °C) = 87.7 kJ mol$^{-1}$ (Figure 2.10, Table 1, Table 2). Hence, binding of **1** to Zn(II) in moto-MOF is unlikely to have a significant effect on the rotary behaviour of motor.

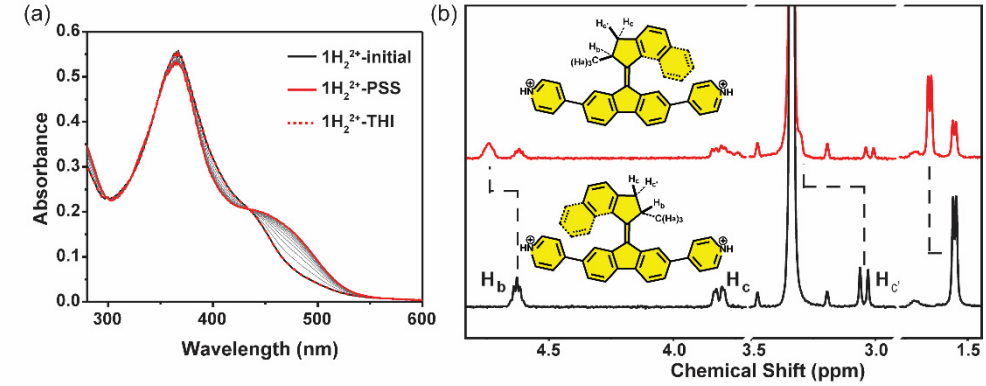


***Figure 2.10*** *(**a**) Changes in UV/Vis spectra of* ***1***$H_2^{2+}$ *upon irradiation with a 395 nm LED. Stable (black solid line), PSS mixture (red solid line), after THI (red dashed line). (**b**) Comparison of* $^1$*H NMR (500 MHz) spectra of protonated stable* ***1*** *(red, bottom spectra) and PSS mixture (purple, top spectra) at -30 °C in* $d_4$*-MeOH. A PSS ratio of 68:32 (metastable:stable) was determined by integration of the aliphatic signals of metastable form and stable form.*

Similarly, the spectroscopic properties of desymmetrized model compound **2**, for which all stereoisomers were identified with $^1$H NMR, excludes possible thermal *E*/*Z* isomerization pathways and confirms that these pyridyl functionalized compounds behave as unidirectional rotary molecular motors (Figure 2.11). The Raman spectrum of stable **1** in $CHCl_3$ showed a sharp band centred at 1562 cm$^{-1}$, which is characteristic[45] of the stretching of the overcrowded olefinic bond. Upon irradiation at 395 nm, an additional band appeared at 1550 cm$^{-1}$ characteristic[45] of the stretching of the central double bond of the metastable isomer (Figure 2.12a). The gradual decrease of this band corresponds to the thermal helix inversion and was followed over time. The rate constant ($k$ = 8.8·10$^{-4}$ s$^{-1}$) at room temperature was used to calculate the activation barrier $\Delta^{\ddagger}G$(20 °C) = 88.9 kJ mol$^{-1}$ (Table 1, Table 2). The value obtained by Raman spectroscopic analysis is in good agreement with the barrier determined by UV/Vis absorption spectroscopy ($\Delta^{\ddagger}G_{CHCl_3}$(20 °C) = 89.1 kJ mol$^{-1}$).

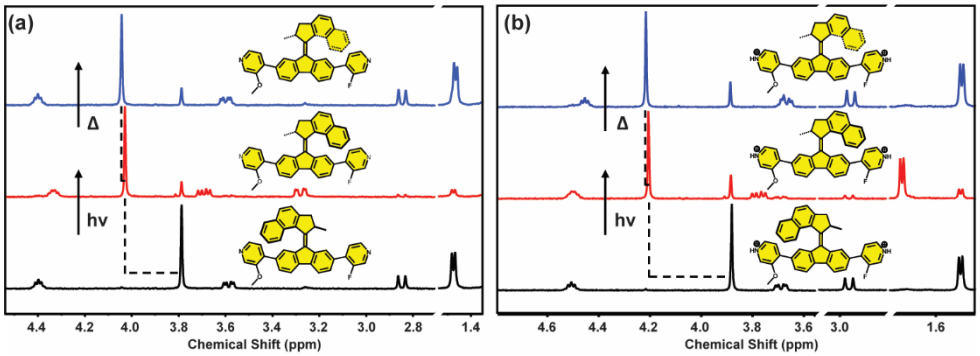


***Figure 2.11*** *(**a**) Comparison of $^{1}$H NMR spectra (500 MHz) of stable **2-E** (black spectra), PSS mixture (red spectra) and PSS mixture kept in the room temperature in dark overnight (blue spectra ) at -30 °C in $CDCl_3$. A PSS ratio of 87:13 (**2-Z** metastable:**2-E** stable) was determined by integration of the aliphatic signals of the metastable form and stable form. Ratio of **2-Z** stable:**2-E** stable (87:13) after THI isomerization of **2-E** metastable was determined by integration of the signals of the methoxy group of the corresponding isomers. (**b**) Comparison of $^{1}$H NMR (500 MHz) spectra of stable **2-E**$H_2^{2+}$ (black spectra), PSS mixture (red spectra) and PSS mixture kept in the room temperature in dark overnight (blue spectra) at -30 °C in $d_4$-MeOH. A PSS ratio of 79:21 (protonated **2-Z** metastable:**2-E** stable) was determined by integration of the aliphatic signals of metastable form and stable form. Ratio of protonated **2-Z** stable:**2-E** stable (79:21) after THI isomerization of protonated **2-Z**$_{meta}$ was determined by integration of the signals of the methoxy group of the corresponding isomers. As it is evident from the ratios of the isomers, heating of the sample to room temperature results in full conversion of the metastable **2-E** into **2-E** stable, thereby completely excluding the TEZ isomerization path for both deprotonated and protonated motor.*

Additionally, the unidirectional rotary motion of the desymmetrized analogue **2** was followed by Raman spectroscopy in $CHCl_3$. The respective **2**-***E***/***Z*** isomers could be identified quantitatively from the intensity of bands in the 1290 $cm^{-1}$ region (Figure 2.12b-d).

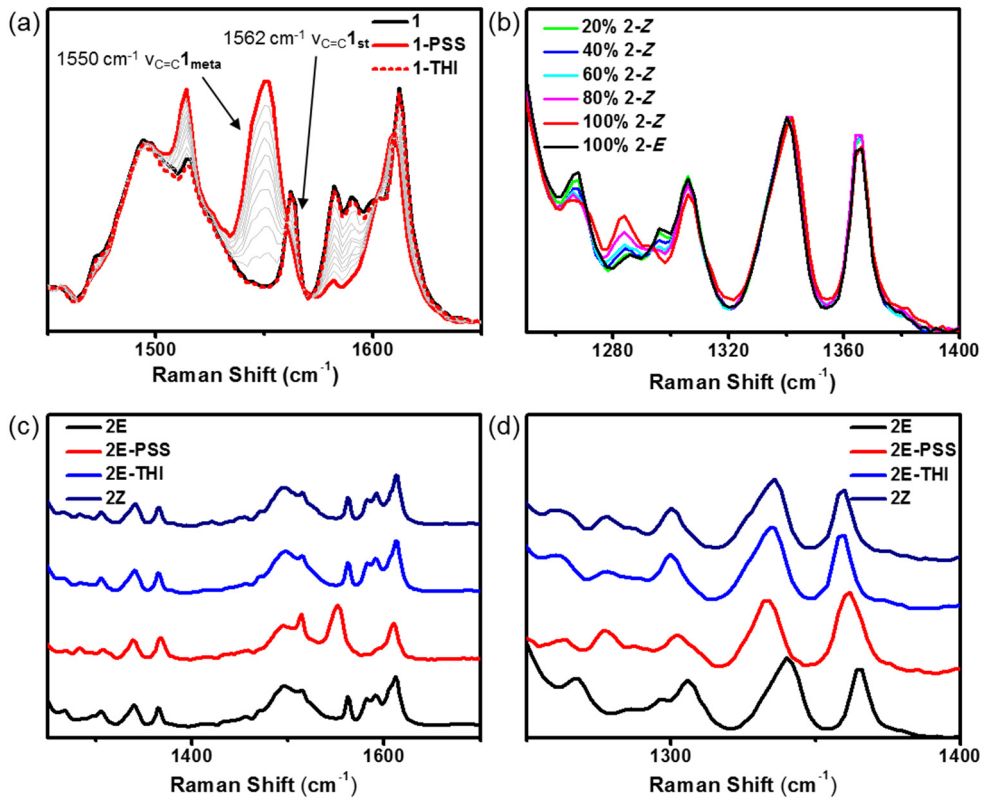


***Figure 2.12*** *(**a**) selected region of the Raman spectrum (785 nm, 50 mW, $3 \cdot 10^{-3}$ M in $CHCl_3$) of stable **1** (black line); after irradiation at 395 nm at -30 °C a new broad band centred at 1550 $cm^{-1}$ is present corresponding to the metastable isomer (red line, **1**-PSS), and after thermal helix inversion the initial spectrum was recovered (red dashed line, **1**-THI). (**b**) Comparison of Raman (785 nm, 50 mW) spectra of various mole fraction mixtures of **2-E** and **2-Z** solutions (total concentration 1.5 mg $ml^{-1}$ in $CHCl_3$). (**c**) Comparison of Raman spectra of **2-Z** (black line), after irradiation at 395 nm for 5 h at -25 °C (PSS mixture, red line), and after THI (blue line). The Raman spectrum of **2-E** (navy line) is shown for comparison. (**d**) Expansion of the Raman spectra from **c** panel in the region 1250-1450 $cm^{-1}$.*

## 2.5 Photochemical and thermal isomerization in the solid state.

The rotary behaviour of molecular motor **1** in the confined environment of the moto-MOF (Figure 2.13a) was studied with Raman spectroscopy. This technique is particularly convenient, as it allows for *in situ* monitoring of structural changes of the individual molecular components in the framework (i.e. molecular motor,

**TCPB**). As it is known for this particular family of MOFs, solvent removal leads to the collapse of the porous structure[42,46] and experiments were therefore performed on moto-MOF crystals immersed in DMF. Photoswitchable MOFs, for example bearing azobenzene[47,48] or diarylethylene[49,50] struts have recently been studied and proven to be stable upon exposure to UV light.[51] Nevertheless, the stability of the framework upon irradiation at 395 nm was verified with PXRD, which showed no changes even over 5 h (see Experimental Data section). Also, no leakage of the linkers to the solution took place as Raman spectra of the solvent only showed bands corresponding to DMF, while the spectra of the single crystals of moto-MOF**1** showed the bands corresponding to the components of the framework. During irradiation of a crystal at 395 nm at room temperature, a gradual decrease in the area of the band at 1562 $cm^{-1}$ was observed, accompanied by a gradual increase of the broad band centred at 1550 $cm^{-1}$ (Figure 2.13b).

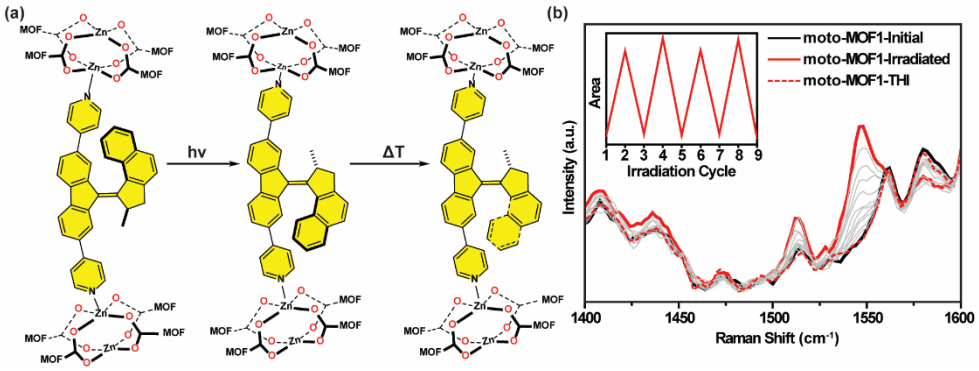


***Figure 2.13*** *(**a**) Schematic representation of structural changes during the photochemical and subsequent thermal isomerization (half of the rotary cycle) of **1** incorporated in moto-MOF**1**. (**b**) Changes in Raman spectrum of moto-MOF**1** (black solid line, initial), upon irradiation at 395 nm (red solid line) and upon subsequent thermal isomerization (red dashed line) at 20 °C, inset shows multiple irradiation/thermal helix inversion cycles, (all Raman spectra were recorded at 785 nm with power density sufficient to avoid sample heating, see Experimental Data section).*

These spectral changes correspond well to those observed in solution and can be therefore ascribed to the same isomerization process. Furthermore, irradiation of moto-MOF**1** crystals at low temperature (-5 °C) showed that, depending, on the crystal thickness, the metastable to stable isomers ratio in moto-MOF**1** can be as high as in solution (see Experimental Data section). Hence, the molecular motors can still undergo their usual photoisomerization when embedded in the MOF. When irradiation was discontinued and the sample was kept in the dark, the band characteristic of the metastable isomer disappeared and the original spectrum was

recovered, indicating that thermal relaxation to the stable isomer had taken place (Figure 2.13b). These irradiation and thermal relaxation steps could be repeated multiple times without any noticeable signs of fatigue (Figure 2.13b, inset). Additionally, for moto-MOF**2**-***E***/***Z*** the changes in intensity around 1290 $cm^{-1}$ upon prolonged irradiation were followed by Raman microscopy. The spectral features in this area are characteristic of the **2**-***E*** and **2**-***Z*** isomers. The same Raman spectrum was obtained upon prolonged irradiation at 395 nm (1 h) of either moto-MOF**2**-***E*** or moto-MOF**2**-***Z*** corresponding to a 1:1 ratio of **2**-***E***/***Z*** pillars, thereby indicating the unidirectional motion of the molecular motor (Figure 2.14). Furthermore, the $^{1}$H NMR spectroscopy of digested crystals of both moto-MOF**2**-***Z*** and moto-MOF**2**-***E*** revealed that the irradiation and subsequent heating to induce thermal helix inversion results in the conversion of the respective pillars into the opposite geometrical isomer (**2**-***E*** and **2**-***Z***, respectively), further corroborating unidirectional rotation of the molecular motor (see Experimental Data section). As in solution, the thermal isomerization of the metastable isomer in both moto-MOF**1** and moto-MOF**2**-***Z*** was followed in time by monitoring the decrease of the band area at 1550 $cm^{-1}$. The barrier ($\Delta^{\ddagger}G$) of thermal helix inversion at room temperature in the moto-MOFs determined was 88.6±0.7 kJ $mol^{-1}$ for moto-MOF**1** and 88.9±1.3 kJ $mol^{-1}$ for moto-MOF**2**-***Z***.[52] These values are in excellent agreement with the barrier determined in solution (Table 1), and the good agreement between the barriers for thermal helix inversion of **1** and **2**-***E*** in moto-MOF excludes a thermal *E*/*Z* isomerization pathway, confirming that the unidirectional rotation of the molecular motor is not compromised by confinement in moto-MOF.

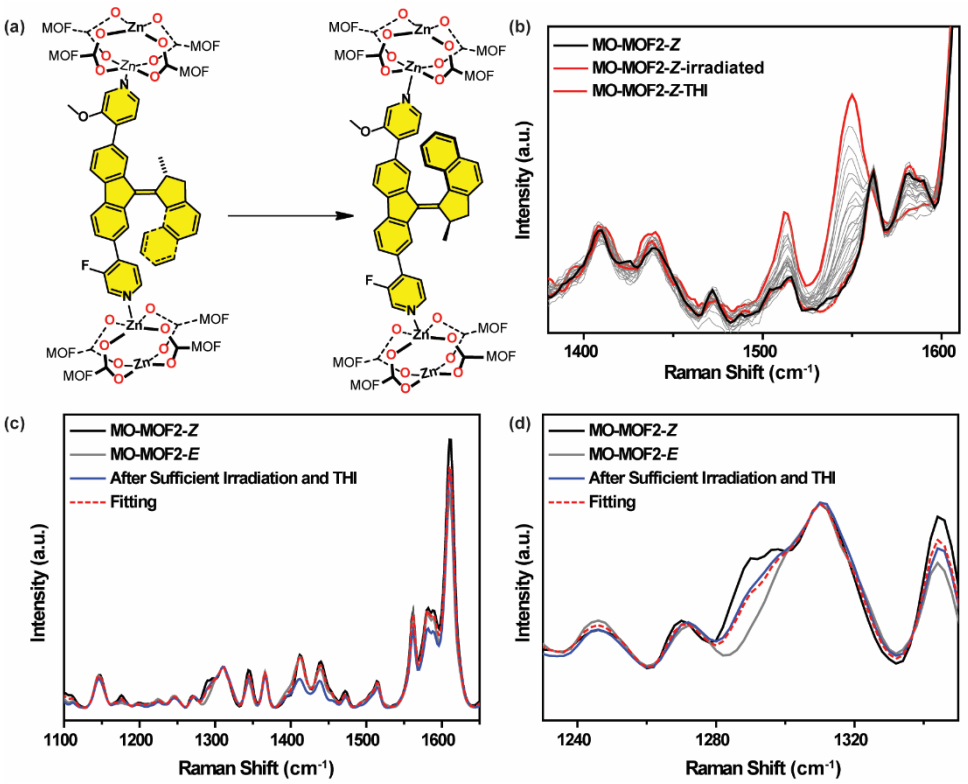


***Figure 2.14*** *(**a**) Schematic representation of structural changes during the photochemical and subsequent thermal isomerization (half of the rotary cycle) of **2-Z** incorporated in moto-MOF**2-Z**. (**b**) Changes in Raman spectrum of moto-MOF**2-Z** (black solid line, initial), upon irradiation at 395 nm (red solid line) and upon subsequent thermal isomerization (red dashed line) at 20 °C. (**c**) Comparison of the Raman spectra of moto-MOF**2-Z** (black line) and moto-MOF**2-E** (grey line) after long irradiation at 395 nm (1 h, 4x$t_{1/2}$, blue line) to reach equal ratio of **2-Z** and **2-E** pillars. The major changes indicative for E/Z isomers are observed around 1290 $cm^{-1}$ (expansion shown at **d** panel). Starting from each isomer moto-MOF**2-Z** or moto-MOF**2-E** same spectrum is obtained (blue line) indicating unidirectional rotation of molecular motor. The green, dashed line is a model spectrum consisting of 50% contribution of moto-MOF**2-Z** and moto-MOF**2-E** spectra. Bands between 1400-1450 $cm^{-1}$ are characteristic of DMF and are not reproducible in the confocal volume of Raman microscope. These spectra were measured for samples kept between two 100 μm-thick sapphire slides at x 100 magnification to minimize the contribution of background.*

## 2.6 Conclusions

In conclusion, we have devised a simple strategy, using SALE, to achieve spatial 3-dimensional organization of light-driven molecular motors using a MOF platform. By using Raman spectroscopy, the photochemically and thermally driven rotary motion in solution could be compared to that in the crystalline solid. It is shown that the motor units in the struts are able to perform unhindered 360° unidirectional rotations, owing to a design which allows for sufficient free volume provided by the chosen framework. These findings are remarkable as it was shown previously that the incorporation of rotaxanes in MOFs influences their dynamics.[36,39] The successful preparation of a fully operational motorized MOF will allow in the future for exploring collective behaviour of 3D-organized rotary molecular motors and tailoring crystalline materials for a specific light-responsive function, for example, control of diffusion of gases, directional light-powered mass transport or for miniature light-powered pumps in microfluidic devices.

## 2.7 Acknowledgments

Jacob Baas is acknowledged for help with acquiring PXRD, Martin Lutz and Edwin Otten for measurement and analysis of SC-X-ray data, Dr. Franco (K.-C.) Leung for making 3D model of the moto-MOF.

## 2.8 Experimental Data

**General Considerations** All reagents were obtained from commercial sources and used as received without further purification. Compounds **3**,[53] **4**,[16] **6**,[41] **DPNI**[42] and **TCPB**[42] were synthesized according to literature procedures. Crystals of the parent Metal Organic Framework were synthesized according to a literature procedure.[42] Dry solvents were obtained from an MBraun solvent purification system. Column chromatography was performed on a Reveleris X2 flash chromatography system. TLC: silica gel 60, Merck, 0.25 mm. HRMS were recorded on an LTQ Orbitrap XL, and Elemental (C, H, N) Analysis was performed on an Elementar vario MICRO cube: Elemental Analyzer, ICP-OES was performed on a PerkinElmer optical emission spectrometer Optima 7000 DV. NMR spectra were obtained using a Varian Mercury Plus ($^{1}$H: 400 MHz, $^{13}$C: 100 MHz $^{19}$F: 376 MHz) or a Varian Innova ($^{1}$H: 500 MHz) instrument. Chemical shifts are reported in δ units (ppm) relative to the residual solvent signal of $CDCl_3$ ($^{1}$H NMR, δ 7.26 ppm; $^{13}$C NMR, δ 77.0 ppm) $d_4$-MeOH ($^{1}$H NMR, δ 3.31 ppm; $^{13}$C NMR, δ 49.0 ppm) or $d_6$-DMSO ($^{1}$H NMR, δ 2.50 ppm; $^{13}$C NMR, δ 39.5 ppm). The splitting pattern of peaks is designated as follows: s (singlet), d (doublet), t (triplet), m (multiplet), br (broad), p (quintet), dd (doublet of doublets) or ddd (doublet of doublet of doublets).

UV/Vis absorption spectra were measured on a Hewlett-Packard 8453 diode array spectrometer in a 1 cm quartz cuvette. Solvents used for spectroscopic studies were of spectroscopic grade (UVASOL, Merck*)*. UV/Vis irradiation experiments were performed using Thorlab LED (M395F1). NMR irradiation experiments were performed at -30 °C with a Thorlab model M395F1 LED coupled to a 0.6 mm optical fiber, which guided the light into the NMR tube inside the spectrometer.[54] Raman spectra were recorded using a Perkin Elmer Raman Station connected to a microscope equipped with a 785 nm 50 mW laser. Raman irradiation experiments were performed using Thorlab LEDs (M395F1). PXRD data were obtained for the capillary-encapsulated samples at room temperature with a Bruker D8 Advance diffractometer equipped with a CuKα source ($\lambda$ = 0.15406 nm). Samples were mounted in capillaries with supernatant liquid; capillaries were sealed with wax and placed on the goniometer head for mounting on the diffractometer. SC X-ray data was collected using Bruker Proteum diffractometer with rotating anode and Cu radiation and Helios optics ($\lambda$ = 1.54184 Å) at a temperature of 100 K. Density functional theory (DFT) calculations were carried out with the Gaussian 09 program (rev. D.01).[55] All of the calculations were performed on systems in the gas phase using the Becke's three-parameter hybrid functional[56] with the LYP correlation functional[57,58] (DFT B3LYP/6-31G(d,p)). Each geometry optimization was followed by a vibrational analysis to determine that a minimum or saddle point on the potential energy surface was found.

**Irradiation Experiments**: For solid state Raman spectroscopy, samples of moto-MOF crystals were kept at room temperature, in 1 mm capped, quartz cuvette filled with DMF or between two quartz slides sealed with PTFE paste to avoid drying. Raman spectra were acquired using a RamanStation400F (PerkinElmer) employing multi-mode fibres for both excitation and emission. Sample was placed on the Olympus BX51 microscope stage and a chosen single crystal of moto-MOF was aligned with laser beam (785 nm, 50 mW) at x 50 lens magnification. Irradiations were carried with 395 nm LED (Thorlab M395F1) connected to 0.6 mm optical fibre, which guided the light to the position of the laser beam.

**Kinetic Measurements** UV/Vis samples in heptane, chloroform or DMF ($\sim 1\times10^{-5}$ M) were irradiated with a Thorlab LED (M395F1) between 7 and 16 °C to reach PSS. The thermal helix inversion was followed by recording UV/Vis spectra with 30-120 s intervals. The absorbance at 480 nm was followed in time in order to extract the rate constants used for the Eyring plots. A least squares analysis was performed on the Eyring equation.

**Kinetic Measurements in moto-MOFs** Crystals of **moto-MOFs** closed in a 1 mm quartz cuvette filled with DMF or between two quartz slides, were irradiated with a Thorlab LED (M395F1) at 20 °C on the microscope stage until no changes were

observed in the Raman spectrum. The thermal helix inversion was followed by recording Raman spectra with 1-5 min intervals. The changes in the area of the band centered at 1550 $cm^{-1}$ was followed in time in order to determine the rate constant and Gibbs free energy of activation of THI.

**2,7-dibromo-9-(2-methyl-2,3-dihydro-1*H*-cyclopenta[a]naphthalen-1-ylidene)-9*H*-fluorene (5)**

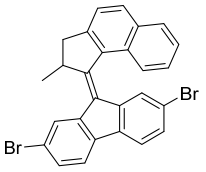


A two-neck flask was charged with 2,7-dibromo-9-diazo-9*H*-fluorene (**3**) (1.0 equiv., 690 mg, 1.97 mmol) and a solution of thioketone **4** (1.3 equiv., 550 mg, 2.59 mmol) in dry THF (20 mL) was added. The reaction mixture was stirred at room temperature for 16 h. Subsequently, tris(dimethylamino)-phosphine (1.29 g, 7.90 mmol, 1.4 mL) was added and the resulting mixture was stirred at room temperature for 16 h and purified by column chromatography ($SiO_2$, pentane/$CH_2Cl_2$) to yield **5** as a yellow solid (720 mg, 1.43 mmol, 73%). $^1$H NMR ($CDCl_3$, 400 MHz): δ 8.08 (d, *J* = 1.6 Hz, 1H), 7.98 (dd, *J* = 8.3 Hz, 2.0 Hz, 2H), 7.70 – 7.45 (m, 6H), 7.47 – 7.34 (m, 1H), 7.33 (dd, *J* = 8.1 Hz, 1.8 Hz, 1H), 6.75 (d, *J* = 1.7 Hz, 1H), 4.30 (p, *J* = 6.6 Hz, 1H), 3.59 (dd, *J* = 15.2 Hz, 5.6 Hz, 1H), 2.82 (d, *J* = 15.2 Hz, 1H), 1.41 (d, *J* = 6.7 Hz, 3H); $^{13}$C NMR (100 MHz, $CDCl_3$): δ 154.2, 148.1, 141.1, 138.3, 137.6, 137.0, 135.2, 132.5, 131.8, 129.5, 129.4, 129.3, 128.9, 128.8, 127.8, 127.0, 126.9, 126.8, 125.5, 123.8, 120.9, 120.7, 119.9, 119.9, 45.1, 41.8, 19.2; HRMS (ESI) calcd $C_{27}H_{19}Br_2$ $[M+H]^+$ 502.9827 found 502.9830.

**Synthesis of 4,4'-(9-(2-methyl-2,3-dihydro-1*H*-cyclopenta[a]naphthalen-1-ylidene)-9*H*-fluorene-2,7-diyl)dipyridine (1)**

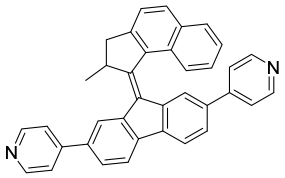


A two-neck round-bottom flask equipped with a reflux condenser was charged with **5** (1.0 equiv., 400 mg 0.80 mmol), 4-pyridinylboronic acid (2.2 equiv., 216 mg, 1.76 mmol) and $Pd(PPh_3)_4$ (0.05 eq., 46 mg, 0.04 mmol). A degassed (by bubbling with the nitrogen for 20 min) aqueous solution of $K_2CO_3$ (1 M, 7.9 mL) and THF (15 mL) were added and the resulting mixture was heated at reflux and stirred at this temperature for 16 h. Subsequently, the reaction mixture was cooled to room temperature, after which EtOAc (30 mL) was added and the aqueous phase was extracted with EtOAc (2 x 10 mL). The combined organic layers were washed with brine (20 mL), dried over $MgSO_4$ and concentrated *in vacuo*, and the crude product was purified by column chromatography ($SiO_2$, pentane/EtOAc) to afford **1** as yellow solid (0.60 mmol, 299 mg, 75%).$^1$H NMR ($CDCl_3$, 400 MHz): δ 8.78 – 8.70 (m, 2H), 8.38 – 8.27 (m, 3H), 8.09 (d, *J* = 8.2 Hz, 1H), 7.99 (t, *J* = 7.8 Hz, 2H), 7.87 (dd, *J* = 13.2 Hz, 8.2 Hz, 2H), 7.71 (dd, *J* = 7.9, 1.5 Hz, 1H), 7.67 – 7.50 (m, 5H), 7.41 (ddd, *J* = 8.2,

6.8, 1.3 Hz, 1H), 7.05 (d, *J* = 1.5 Hz, 1H), 6.66 – 6.60 (m, 2H), 4.45 (p, *J* = 6.6 Hz, 1H), 3.62 (dd, *J* = 15.3 Hz, 5.7 Hz, 1H), 2.86 (d, *J* = 15.3 Hz, 1H), 1.52 (d, *J* = 6.7 Hz, 3H) $^{13}$C NMR (100 MHz, $CDCl_3$): δ 152.8, 150.2, 149.7, 148.8, 147.9, 147.9, 140.8, 139.9, 139.2, 137.9, 137.1, 135.6, 135.6, 132.6, 131.6, 129.7, 129.3, 129.0, 127.2, 127.0, 125.8, 125.4, 125.2, 124.4, 124.1, 122.6, 121.4, 120.8, 120.5, 119.7, 45.1, 41.8, 19.2. HRMS (ESI) calcd $C_{37}H_{27}N_2$ $[M+H]^+$ 499.2169 found 499.2167.

**(*E*/*Z*) *N*'-(2-bromo-7-iodo-9*H*-fluoren-9-ylidene)-4-methylbenzenesulfonohydrazide (7)**

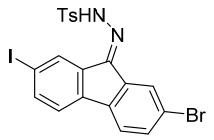


A two-neck round-bottom flask was charged with 2-bromo-7-iodo-9*H*-fluoren-9-one (**6**) (1.0 equiv., 2.00 g, 5.19 mmol) and *p*-toluenesulfonyl hydrazide (1.2 equiv., 1.16 g, 6.23 mmol) and EtOH (100 mL) was added. The resulting suspension was heated at reflux and stirred at this temperature for 16 h. The reaction mixture was cooled down to room temperature and the precipitate was filtrated, washed with EtOH (30 mL) and dried to afford **7** as a pale yellow solid (*E*/*Z* mixture 1/1 ratio, 2.80 g, 5.10 mmol, 98%).The product was used in the next reaction step without further purification. $^1$H NMR (400 MHz, $d_6$-DMSO): δ 8.38 (s, 1H) 8.22 (s, 1H), 7.97 – 7.83 (m, 5H), 7.83 – 7.51 (m, 10H), 7.46 (d, *J* = 8.0 Hz, 5H), 2.38 (s, 6H). HRMS (ESI) calcd $C_{20}H_{15}BrNISO_2$ $[M+H]^+$ 552.9077 found 552.9085.

**2-bromo-9-diazo-7-iodo-9*H*-fluorene (8)**

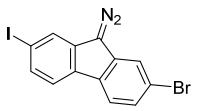


A round-bottom flask was charged with *N*-tosylhydrazone **7** (2.00 g 3.61 mmol) and an aqueous solution of NaOH (2 M, 100 mL) was added. The resulting suspension was heated at 90 °C and stirred at this temperature for 16 h. The resulting suspension was cooled down to room temperature and the aqueous phase was extracted with $CH_2Cl_2$ (3 x 100 mL). The combined organic layers were washed with brine (150 mL), dried over $MgSO_4$ and concentrated *in vacuo*. The pure product was obtained by crystallization from $Et_2O$ to afford **8** as pink needle-shaped crystals (1.10 g, 2.70 mmol, 75%) $^1$H NMR (400 MHz, $CDCl_3$): δ 7.82 (t, *J* = 1.0 Hz, 1H), 7.75 (d, *J* = 8.2 Hz, 1H), 7.62 (dd, *J* = 2.7 Hz, 1.4 Hz, 3H), 7.43 (dd, *J* = 8.3 Hz, 1.7 Hz, 1H). $^{13}$C NMR (100 MHz, $CDCl_3$) δ 134.5, 134.1, 133.4, 129.7, 129.2, 127.8, 127.7, 122.2, 122.0, 121.8, 120.5, 91.3. (Resonance corresponding to carbon connected to diazo moiety was not observed).

**(*E*/*Z*)-2-bromo-7-iodo-9-(2-methyl-2,3-dihydro-1*H*-cyclopenta[a]naphthalen-1-ylidene)-9*H*-fluorene (9)**

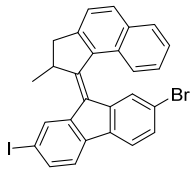


A two-neck flask was charged with 2-bromo-9-diazo-7-iodo-9*H*-fluorene (**8**) (1.0 equiv., 794 mg, 2.00 mmol) and a solution of thioketone **4** (1.3 equiv., 552 mg, 2.60 mmol) in dry THF (20 mL) was added. The reaction mixture was stirred at room temperature for 16 h. Subsequently tris(dimethylamino)-phosphine (4 equiv., 1.30 g, 8.00 mmol, 1.4 mL) was added and the resulting mixture was stirred at room temperature for 16 h. After purification by column chromatography ($SiO_2$, pentane/$CH_2Cl_2$) **9** was obtained as a yellow solid (*E*/*Z* mixture 1/1.1 ratio, 760 mg, 1.38 mmol, 69%). $^1$H NMR (400 MHz, $CDCl_3$) δ 8.30 (d, *J* = 1.4 Hz, 1H), 8.08 (d, *J* = 1.6 Hz, 1H), 7.97 (dd, *J* = 7.1 Hz, 2.9 Hz, 4H), 7.76 – 7.29 (m, 16H), 6.94 (d, *J* = 1.4 Hz, 1H), 6.75 (d, *J* = 1.6 Hz, 1H) 4.29 (q, *J* = 5.9 Hz, 2H), 3.58 (dd, *J* = 15.2, 5.6 Hz, 2H), 2.81 (d, *J* = 15.2 Hz, 2H), 1.41 (m, *J* = 6.8 Hz, 3.6 Hz, 6H). $^{13}$C NMR (101 MHz, $CDCl_3$) δ 154.1, 148.1, 148.1, 141.4, 140.8, 138.4, 138.1, 138.0, 137.7, 137.5, 137.1, 135.4, 135.2, 135.0, 133.0, 132.5, 132.5, 131.8, 131.8, 129.5, 129.4, 129.3, 129.2, 128.8, 127.7, 127.6, 126.9, 126.9, 126.8, 126.8, 125.5, 125.5, 123.8, 123.7, 121.1, 121.0, 120.7, 120.2, 120.1, 119.9, 92.3, 91.2, 45.1, 45.0, 41.8, 41.8, 19.2, 19.1. HRMS (APCI neg.) calcd $C_{27}H_{17}BrI$ $[M-H]^-$ 546.9553 found 546.9553.

**(*E*)/(*Z*)-4-(7-bromo-9-(2-methyl-2,3-dihydro-1*H*-cyclopenta[a]naphthalen-1-ylidene)-9*H*-fluoren-2-yl)-3-fluoropyridine (10-*E*), (10-*Z*)**

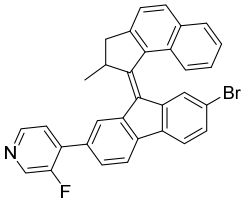


A two-neck round-bottom flask equipped with a reflux condenser was charged with a *E*/*Z* (1/1.1 ratio) mixture of **9** (1.0 equiv., 505 mg 0.92 mmol), 3-fluoro-4-pyridineboronic acid pinacol ester (1.09 equiv., 225 mg, 1.0 mmol), and $Pd(dppf)Cl_2$•$CH_2Cl_2$ (0.05 eq., 38 mg, 0.046 mmol). A degassed (by bubbling with the nitrogen for 20 min.) aqueous solution of $K_2CO_3$ (1 M, 10 equiv., 9.2 mL) and THF (10 mL) were added and the resulting mixture was stirred at reflux for 5 h. Subsequently, the reaction mixture was cooled to room temperature, diluted with EtOAc (20 mL) and the phases were separated. The aqueous phase was extracted with EtOAc (2 x 10 mL) and the combined organic layers were washed with brine (20 mL), dried over $MgSO_4$ and concentrated *in vacuo*. Purification by column chromatography, during which the *E*-*Z* isomers could be readily separated, ($SiO_2$ pentane/EtOAc) afforded **10-*E*** and **10-*Z*** as yellow solids (0.38 mmol, 197 mg, 87% **10-*E***, 0.40 mmol, 207 mg, 83% **9-*Z***). **10-*E***: $^1$H NMR (400 MHz, $CDCl_3$) δ 8.30 (d, *J* = 2.7 Hz, 1H), 8.12 (d, *J* = 1.6 Hz, 1H), 8.05 (dd, *J* = 9.3 Hz, 6.6 Hz, 2H), 7.96 (d, *J* = 8.2 Hz, 1H), 7.86 – 7.72 (m, 3H), 7.63 – 7.51 (m, 4H), 7.41 (ddd, *J* = 8.2 Hz, 6.8 Hz, 1.3 Hz,

1H), 6.90 (d, *J* = 1.5 Hz, 1H), 6.14 (dd, *J* = 6.9, 5.0 Hz, 1H), 4.32 (p, *J* = 6.6 Hz, 1H), 3.59 (dd, *J* = 15.3 Hz, 5.6 Hz, 1H), 2.82 (d, *J* = 15.3 Hz, 1H), 1.44 (d, *J* = 6.7 Hz, 3H). $^{13}$C NMR (100 MHz, $CDCl_3$) δ 153.4, 148.1, 145.4, 145.3, 141.7, 139.0, 138.6, 138.3, 137.8, 137.1, 135.5, 132.6, 131.6, 131.5, 131.2, 130.4, 130.3, 129.7, 129.7, 129.0, 128.7, 127.9, 127.8, 127.0, 127.0, 125.6, 124.0, 123.5, 121.3, 121.2, 118.9, 45.0, 41.9, 19.1. (more signals were observed due to coupling to $^{19}$F). $^{19}$F NMR (376 MHz, $CDCl_3$): -132.82 (d). HRMS (ESI) calcd $C_{32}H_{22}BrNF$ $[M+H]^+$ 518.0914 found 518.0911. **10-*Z***: $^1$H NMR (400 MHz, $CDCl_3$) δ 8.60 (s, 1H), 8.53 (d, *J* = 4.9 Hz, 1H), 8.29 (s, 1H), 8.02 – 7.90 (m, 3H), 7.71 – 7.57 (m, 4H), 7.58 – 7.49 (m, 2H), 7.46 – 7.34 (m, 2H), 6.80 (d, *J* = 1.7 Hz, 1H), 4.38 (p, *J* = 6.6 Hz, 1H), 3.61 (dd, *J* = 15.3 Hz, 5.7 Hz, 1H), 2.83 (d, *J* = 15.2 Hz, 1H), 1.44 (d, *J* = 6.7 Hz, 3H), $^{13}$C NMR (100 MHz, $CDCl_3$) δ 153.9, 148.0, 145.8, 145.7, 139.7, 139.7, 139.0, 138.9, 138.7, 137.1, 136.7, 136.6, 135.3, 132.5, 131.8, 131.3, 131.3, 129.5, 129.3, 129.0, 128.8, 128.3, 127.3, 127.2, 126.9, 126.8, 125.5, 124.6, 124.6, 123.8, 120.4, 120.3, 119.9, 45.3, 41.8, 19.2. $^{19}$F NMR (376 MHz, $CDCl_3$): -132.57 (br). HRMS (ESI) calcd $C_{32}H_{22}BrFN$ $[M+H]^+$ 518.0914, found 518.0920.

**(*E*)/(*Z*)-3-fluoro-4-(7-(3-methoxypyridin-4-yl)-9-(2-methyl-2,3-dihydro-1*H*-cyclopenta[a]naphthalen-1-ylidene)-9*H*-fluoren-2-yl)pyridine (2-*E*), (2-*Z*)**

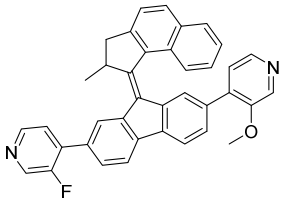


A two-neck round-bottom flask equipped with a reflux condenser was charged with **10-*E*** or **10-*Z*** (1.0 equiv., 119 mg 0.23 mmol), 3-methoxy-4-pyridineboronic acid pinacol ester (1.4 equiv., 75 mg, 0.32 mmol) and $Pd(PPh_3)_4$ (0.05 equiv., 13 mg, 0.012 mmol). A degassed (by bubbling with the nitrogen for 20 min.) aqueous solution of $K_2CO_3$ (1 M, 2.3 mL) and THF (10 mL) were added and the resulting mixture was stirred at reflux for 2 h. Subsequently, the reaction mixture was cooled to room temperature, diluted with EtOAc (10 mL) and the phases were separated. The aqueous phase was extracted with EtOAc (2 x 10 mL) and the combined organic layers were washed with brine (20 mL), dried over $MgSO_4$ and concentrated *in vacuo*. Purification by column chromatography ($SiO_2$ pentane/EtOAc) afforded **2-*E*** and as yellow solid (0.18 mmol, 98 mg, 78 % **2-*E***). **2-*Z*** was synthesized according to the same procedure (0.19 mmol, 104 mg, 83 % **2-*Z***). **2-*E***: $^1$H NMR (400 MHz, $CDCl_3$) δ 8.61 (d, *J* = 2.7 Hz, 1H), 8.53 (dd, *J* = 5.0, 0.8 Hz, 1H), 8.31 (s, 1H), 8.16 (s, 1H), 8.04 – 7.82 (m, 6H), 7.66 (ddd, *J* = 10.4 Hz, 7.9 Hz, 1.5 Hz, 2H), 7.56 (ddd, *J* = 9.7 Hz, 7.6 Hz, 5.7 Hz, 3H), 7.43 (ddd, *J* = 8.3 Hz, 6.8 Hz, 1.3 Hz, 1H), 6.89 (d, *J* = 1.4 Hz, 1H), 6.17 (d, *J* = 4.8 Hz, 1H), 4.38 (p, *J* = 6.6 Hz, 1H), 3.71 (s, 3H), 3.59 (dd, *J* = 15.2 Hz, 5.6 Hz, 1H), 2.81 (d, *J* = 15.2 Hz, 1H), 1.46 (d, *J* = 6.7 Hz, 3H). $^{13}$C NMR (100 MHz, $CDCl_3$) δ 157.9, 152.5, 152.2, 147.7, 146.0, 145.9, 142.6, 140.4, 140.2, 139.2, 138.9, 138.3,

137.6, 137.3, 136.5, 136.4, 135.8, 134.1, 133.6, 132.6, 131.3, 129.8, 129.5, 129.0, 128.3, 127.3, 127.3, 127.1, 126.9, 126.1, 125.0, 124.6, 124.5, 124.0, 123.9, 123.8, 120.1, 118.7, 56.0, 45.2, 41.9, 19.2. (more signals were observed due to coupling to $^{19}$F). $^{19}$F NMR (376 MHz, $CDCl_3$): -132.77 (d). HRMS (ESI) calcd $C_{36}H_{28}FN_2O$ $[M+H]^+$ 547.2180, found 547.2161. **2-*Z***: $^1$H NMR (400 MHz, $CDCl_3$) δ 8.48 – 8.37 (m, 2H), 8.32 (dd, *J* = 9.5, 2.1 Hz, 2H), 8.01 (ddd, *J* = 33.2 Hz, 8.2 Hz, 5.4 Hz, 4H), 7.88 (dd, *J* = 8.2, 5.4 Hz, 2H), 7.72 – 7.50 (m, 4H), 7.51 – 7.37 (m, 2H), 6.95 (d, *J* = 1.5 Hz, 1H), 6.15 (dd, *J* = 6.9 Hz, 5.0 Hz, 1H), 4.39 (p, *J* = 6.6 Hz, 1H), 4.00 (s, 3H), 3.59 (dd, *J* = 15.3 Hz, 5.7 Hz, 1H), 2.81 (d, *J* = 15.2 Hz, 1H), 1.44 (d, *J* = 6.7 Hz, 3H). $^{13}$C NMR (100 MHz, $CDCl_3$) δ 152.4, 147.8, 145.4, 145.3, 143.1, 139.9, 139.5, 139.1, 138.6, 138.3, 137.8, 137.7, 135.8, 135.7, 134.6, 134.4, 132.6, 132.0, 131.9, 131.8, 131.4, 130.3, 129.7, 129.6, 129.0, 128.4, 128.3, 127.9, 127.8, 127.8, 127.1, 126.9, 125.6, 125.1, 125.1, 124.2, 124.0, 123.5, 119.9, 119.1, 56.2, 45.1, 41.9, 19.2. (more signals were observed due to coupling to $^{19}$F) $^{19}$F NMR (376 MHz, $CDCl_3$): -132.77 (m). HRMS (ESI) calcd $C_{36}H_{28}FN_2O$ $[M+H]^+$ 547.2180 found 547.2183.

**Synthesis of moto-MOF via SALE** Crystals of parent BrYO-MOF[42] (30 mg) were placed in a 2 mL screw cap vial and a 1 mL solution of motor **1** (30 mg, 0.06 mmol) in DMF was added. Next, the vial was capped and placed in an oven at 60 °C for 24 h. For moto-MOF**2-*Z*** and moto-MOF**2-*E*** similar procedure was used but the exchange was performed on 15 mg of parent BrYO-MOF with a solution of either **2-*E*** or **2-*Z*** (1ml, 30 mg) for 96 h and the exchange solution was replaced with a fresh batch every 24 h. For moto-MOF**2-*E*** the exchange was carried out in a 1:1 (v:v) mixture of NMP/DMF due to low solubility of **2-*E*** in pure DMF. Subsequently, the vial was removed from the oven and the supernatant solution was immediately replaced with 1 mL of fresh DMF. To remove the excess of **1**, the supernatant solution was replaced with fresh portions of DMF after 0.5, 1, 2, 6, 24 and 48 h. For elemental analysis, the MOF crystals were extensively washed with DCM and dried *in vacuo*. For NMR studies, the MOF crystals were extensively washed with DCM, dried *in vacuo*, and the 0.5 mL of $d_6$-DMSO and two drops of $D_2SO_4$ were added. The sample was sonicated until complete dissolution of the MOF crystals was achieved. Elemental analysis moto-MOF**1** calcd. $[C_{71}H_{42}O_8N_2Zn_2Br_2 \cdot 3H_2O]$ %C 61.10; %H 3.47; %N 2.01; %Zn 9.37; found %C 60.87, %H 3.45, %N 2.06, %Zn 9.00

***Table 2.*** *Summary of the thermodynamic parameters of the transition state for the thermal isomerization of* ***1*** *and* $\mathbf{1}H_2^{2+}$ *in various solvents.*

| Solvent | $\Delta^{\ddagger}G$ (20 °C) (kJ mol$^{-1}$) | $\Delta^{\ddagger}H$ (20 C) (kJ mol$^{-1}$) | $\Delta^{\ddagger}S$ (20 °C) (J mol K$^{-1}$) | $t_{1/2}$ (min) |
|---|---|---|---|---|
| Chloroform | 89.1±0.7 | 76.8±2.1 | -42.3±7.4 | 15 |
| Heptane | 89.5±0.2 | 81.9±2.2 | -26.1±7.8 | 7 |
| DMF | 87.7±0.6 | 89.4±2.5 | 5.7±8.7 | 8 |
| DMF $\mathbf{1}H_2^{2+}$ | 87.7±0.2 | 75.4±2.0 | -41.8±7.2 | 8 |

*Errors of the Gibbs free energy were estimated as 95% confidence intervals, errors of entropy and enthalpy were derived from the fit.*

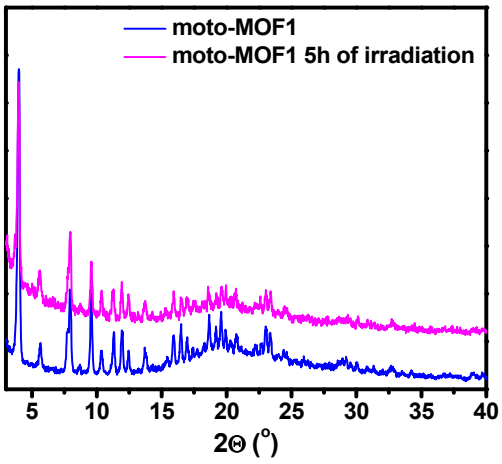


***Figure 2.15*** *PXRD patterns of MOFs, moto-MOF****1*** *after SALE with* ***1*** *(blue line) moto-MOF****1*** *irradiated for 5 h with 395 nm (purple line).*

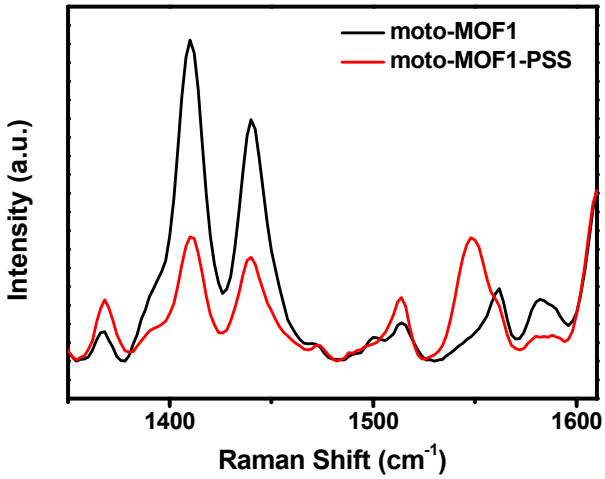


***Figure 2.16*** *Comparison of Raman spectra of thin crystal of moto-MOF**1** before (black spectrum) and after irradiation at (395 nm) -5 °C (red spectrum). The ratio of metastable to stable isomer achieved can be estimated from the ratio of intensities of bands at 1550 $cm^{-1}$ (band characteristic of metastable isomer) to bands and 1582 $cm^{-1}$ (ca. 5) which are similar to the ratio of intensities of these bands in the Raman spectrum of a PSS mixture in $CHCl_3$ (ca. 5). It can be therefore concluded that depending on the crystal thickness the PSS ratio that can be achieved can be as high as in solution (ca. 80-70 % of metastable isomer). Bands around 1400–1500 $cm^{-1}$ are characteristic of DMF and their intensity varies with time depending on exact position of the confocal volume with respect to the crystal.*

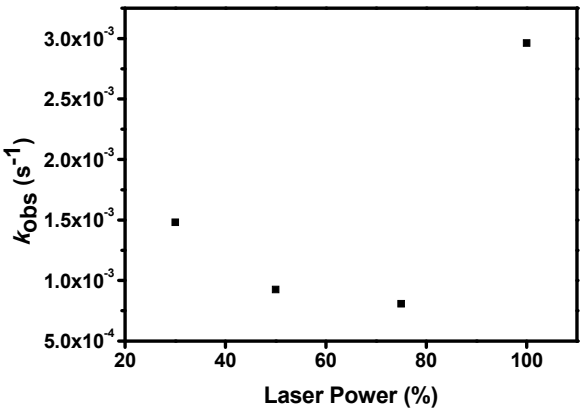


***Figure 2.17*** *Comparison of observed rate constants of* ***1*** *in MOF using 30, 50, 75 and 100% 50 mW 785 nm laser power (30 s exposure time, spectra recorded every 2 min). Decreasing laser power to 75% of its nominal value results in lowering the observed k, further lowering of the laser power does not lead to further lowering of observed k indicating that local heating effect is only observed when 100% laser power is used.*

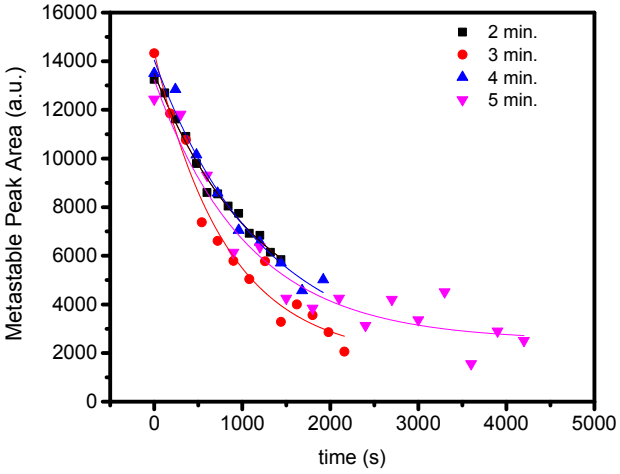


***Figure 2.18*** *Comparison of the exponential decay of the area of the band corresponding to metastable isomer of* ***1*** *in MOF recorded with 75% laser power with different (2 (black squares) 3 (red rectangles), 4 (blue triangles), 5 (purple rectangles) minutes) time intervals between recording consequent Raman spectra (30 s exposure to the laser time, real experiment time). Rate constants were obtained by fitting exponential decay* $I=I_0e^{-kt}+B$ *using Origin software. The values of the rate constant obtained were similar and independent on the interval time, thereby excluding local heating.*

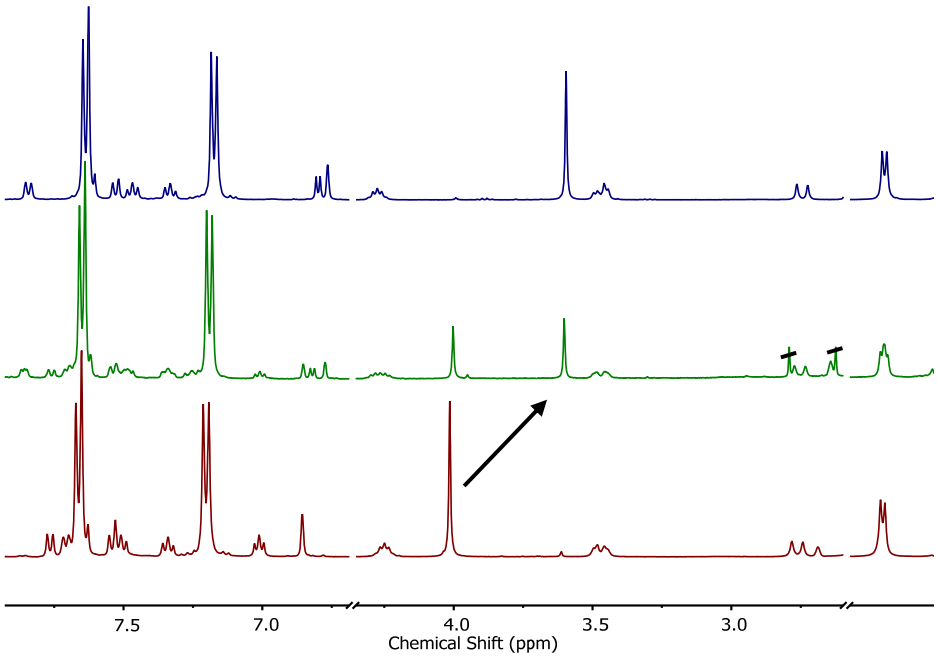


***Figure 2.19*** *Comparison of $^{1}$H NMR ($d_6$-DMSO, digested using $D_2SO_4$) spectra of moto-MOF**2-Z** (black spectrum), and moto-MOF**2-Z** after irradiation at 395 nm and THI (red spectrum). Crystals of moto-MOF**2-Z** were ground in a mortar and irradiated for 4 h at -20 °C with stirring. The crystals were recovered by centrifugation, washed with DCM to remove DMF and dried in vacuo. Upon irradiation, a metastable **2-E** pillar is formed which is subsequently converted to stable **2-Z** thereby showing unidirectional rotation of the motor. The $^{1}$H NMR spectrum of digested moto-MOF**2-E** is shown for comparison. Crossed resonances belong to residual DMF.*

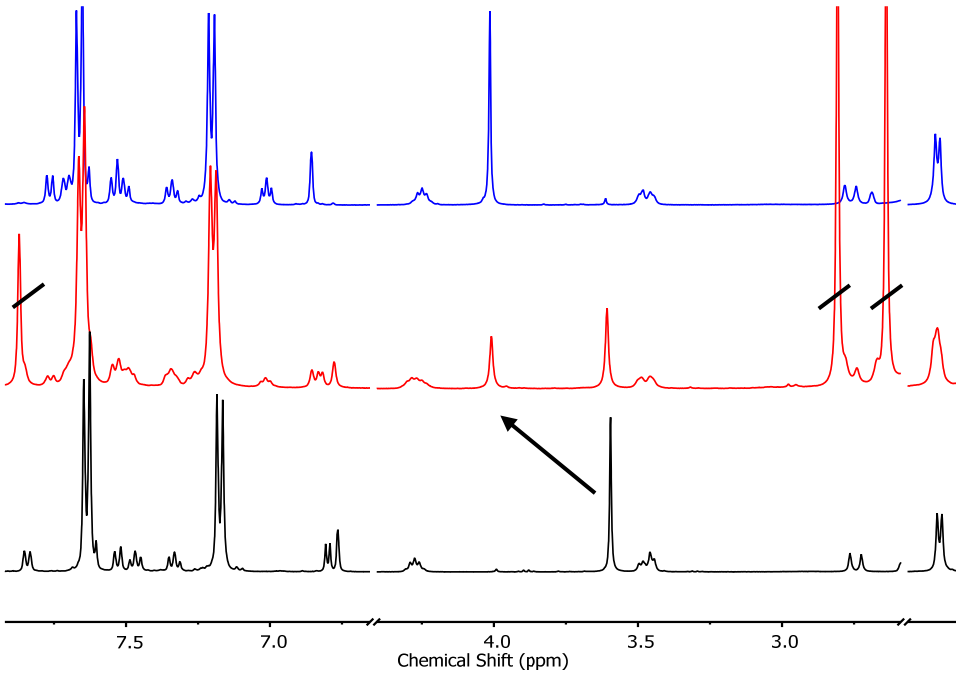


*Figure 2.20 Comparison of $^1$H NMR ($d_6$-DMSO, digested using $D_2SO_4$) spectra of moto-MOF**2-E** (black spectrum), and moto-MOF**2-E** after irradiation at 395 nm and THI (red spectrum). Crystals of moto-MOF**2-E** were ground in a mortar and irradiated for 4 h at -20 °C with stirring. The crystals were recovered by centrifugation, washed with DCM to remove DMF and dried in vacuo. Upon irradiation, a metastable **2-Z** pillar is formed which is subsequently converted to stable **2-E** thereby showing unidirectional rotation of the motor. The final ratio of **2-E**/**2-Z** 60/40 was determined by integration of the methoxy resonances of the respective isomers. The $^1$H NMR spectrum of digested moto-MOF**2-Z** is shown for comparison. Crossed resonances belong to residual DMF.*

## 2.9 References


1 C. Dietrich-Buchecker, M. C. Jimenez-Molero, V. Sartor and J.-P. Sauvage, Rotaxanes and catenanes as prototypes of molecular machines and motors, *Pure Appl. Chem.*, 2003, **75**, 1383–1393.

2 V. Balzani, M. Venturi and A. Credi, *Molecular devices and machines : a journey into the nano world*, Wiley-VCH, 2003.

3 E. R. Kay, D. A. Leigh and F. Zerbetto, Synthetic molecular motors and mechanical machines, *Angew. Chem. Int. Ed.*, 2007, **46**, 72–191.

4 G. Vives, H. P. J. De Rouville, A. Carella, J. P. Launay and G. Rapenne, Prototypes of molecular motors based on star-shaped organometallic ruthenium complexes, *Chem. Soc. Rev.*, 2009, **38**, 1551–1561.

5 S. Erbas-Cakmak, D. A. Leigh, C. T. McTernan and A. L. Nussbaumer, Artificial Molecular Machines, *Chem. Rev.*, 2015, **115**, 10081–10206.

6 R. D. Vale and R. A. Milligan, The way things move: Looking under the hood of molecular motor proteins, *Science*, 2000, **288**, 88–95.

7 K. Kinbara and T. Aida, Toward Intelligent Molecular Machines: Directed Motions of Biological and Artificial Molecules and Assemblies, *Chem. Rev.*, 2005, **105**, 1377–1400.

8 M. Schliwa, *Molecular motors*, Wiley-VCH, Weinheim, 2003.

9 A. Coskun, M. Banaszak, R. D. Astumian, J. F. Stoddart and B. A. Grzybowski, Great expectations: can artificial molecular machines deliver on their promise?, *Chem. Soc. Rev.*, 2012, **41**, 19–30.

10 T. van Leeuwen, A. S. Lubbe, P. Štacko, S. J. Wezenberg and B. L. Feringa, Dynamic control of function by light-driven molecular motors, *Nat. Rev. Chem.*, 2017, **1**, 0096.

11 J. Berná, D. A. Leigh, M. Lubomska, S. M. Mendoza, E. M. Pérez, P. Rudolf, G. Teobaldi and F. Zerbetto, Macroscopic transport by synthetic molecular machines, *Nat. Mater.*, 2005, **4**, 704–710.

12 T. J. Huang, B. Brough, C.-M. Ho, Y. Liu, A. H. Flood, P. A. Bonvallet, H.-R. Tseng, J. F. Stoddart, M. Baller and S. Magonov, A nanomechanical device based on linear molecular motors, *Appl. Phys. Lett.*, 2004, **85**, 5391–5393.

13 N. Koumura, R. W. J. Zijistra, R. A. Van Delden, N. Harada and B. L. Feringa, Light-driven monodirectional molecular rotor, *Nature*, 1999, **401**, 152–155.

14 N. Koumura, E. M. Geertsema, A. Meetsma and B. L. Feringa, Light-driven molecular rotor: Unidirectional rotation controlled by a single stereogenic center, *J. Am. Chem. Soc.*, 2000, **122**, 12005–12006.

15 R. Eelkema, M. M. Pollard, J. Vicario, N. Katsonis, B. S. Ramon, C. W. M. Bastiaansen, D. J. Broer and B. L. Feringa, Nanomotor rotates microscale objects, *Nature*, 2006, **440**, 163.

16 D. Pijper and B. L. Feringa, Molecular transmission: Controlling the twist sense of a helical polymer with a single light-driven molecular motor, *Angew. Chem. Int. Ed.*, 2007, **46**, 3693–3696.

17 D. Pijper, M. G. M. Jongejan, A. Meetsma and B. L. Feringa, Light-Controlled Supramolecular Helicity of a Liquid Crystalline Phase Using a Helical Polymer Functionalized with a Single Chiroptical Molecular Switch, *J. Am. Chem. Soc.*, 2008, **130**, 4541–4552.

18 T. Orlova, F. Lancia, C. Loussert, S. Iamsaard, N. Katsonis and E. Brasselet, Revolving supramolecular chiral structures powered by light in nanomotor-doped liquid crystals, *Nat. Nanotechnol.*, 2018, **13**, 304–308.

19 S. Iamsaard, S. J. Aßhoff, B. Matt, T. Kudernac, J. J. L. M. Cornelissen, S. P. Fletcher and N. Katsonis, Conversion of light into macroscopic helical motion, *Nat. Chem.*, 2014, **6**, 229–235.

20 Q. Li, G. Fuks, E. Moulin, M. Maaloum, M. Rawiso, I. Kulic, J. T. Foy and N. Giuseppone, Macroscopic contraction of a gel induced by the integrated motion of light-driven molecular motors, *Nat. Nanotechnol.*, 2015, **10**, 161–165.

21 J. T. Foy, Q. Li, A. Goujon, J. R. Colard-Itté, G. Fuks, E. Moulin, O. Schiffmann, D. Dattler, D. P. Funeriu and N. Giuseppone, Dual-light control of nanomachines that integrate motor and modulator subunits, *Nat. Nanotechnol.*, 2017, **12**, 540–545.

22 J. Chen, F. K. C. Leung, M. C. A. Stuart, T. Kajitani, T. Fukushima, E. Van Der Giessen and B. L. Feringa, Artificial muscle-like function from hierarchical supramolecular assembly of photoresponsive molecular motors, *Nat. Chem.*, 2018, **10**, 132–138.

23 R. A. Van Delden, M. K. J. Ter Wiel, M. M. Pollard, J. Vicario, N. Koumura and B. L. Feringa, Unidirectional molecular motor on a gold surface, *Nature*, 2005, **437**, 1337–1340.

24 K. Y. Chen, O. Ivashenko, G. T. Carroll, J. Robertus, J. C. M. Kistemaker, G. London, W. R. Browne, P. Rudolf and B. L. Feringa, Control of surface wettability using tripodal light-activated molecular motors, *J. Am. Chem. Soc.*, 2014, **136**, 3219–3224.

25 J. Kaleta, J. Chen, G. Bastien, M. Dračínský, M. Mašát, C. T. Rogers, B. L. Feringa and J. Michl, Surface Inclusion of Unidirectional Molecular Motors in Hexagonal Tris(o-phenylene)cyclotriphosphazene, *J. Am. Chem. Soc.*, 2017, **139**, 10486–10498.

26 H. Deng, M. A. Olson, J. F. Stoddart and O. M. Yaghi, Robust dynamics, *Nat. Chem.*, 2010, **2**, 439–443.

27 R. D. Astumian, How molecular motors work – insights from the molecular machinist's toolbox: the Nobel prize in Chemistry 2016, *Chem. Sci.*, 2017, **8**, 840–845.

28 C. Pezzato, C. Cheng, J. F. Stoddart and R. D. Astumian, Mastering the non-equilibrium assembly and

operation of molecular machines, *Chem. Soc. Rev.*, 2017, **46**, 5491–5507.
29 A. J. Howarth, Y. Liu, P. Li, Z. Li, T. C. Wang, J. T. Hupp and O. K. Farha, Chemical, thermal and mechanical stabilities of metal-organic frameworks, *Nat. Rev. Mater.*, 2016, **1**, 1–15.
30 H. Furukawa, K. E. Cordova, M. O'Keeffe and O. M. Yaghi, The chemistry and applications of metal-organic frameworks, *Science*, 2013, **341**, 1230444.
31 S. L. Gould, D. Tranchemontagne, O. M. Yaghi and M. A. Garcia-Garibay, The Amphidynamic Character of Crystalline MOF-5 : Rotational Dynamics in a Free-Volume Environment, *J. Am. Chem. Soc.*, 2008, **130**, 3246–3247.
32 S. Bracco, T. Miyano, M. Negroni, I. Bassanetti, L. Marchio', P. Sozzani, N. Tohnai and A. Comotti, $CO_2$ regulates molecular rotor dynamics in porous materials, *Chem. Commun.*, 2017, **53**, 7776–7779.
33 S. Bracco, F. Castiglioni, A. Comotti, S. Galli, M. Negroni, A. Maspero and P. Sozzani, Ultrafast Molecular Rotors and Their CO2 Tuning in MOFs with Rod-Like Ligands, *Chem. Eur. J.*, 2017, **23**, 11210–11215.
34 C. S. Vogelsberg, F. J. Uribe-Romo, A. S. Lipton, S. Yang, K. N. Houk, S. Brown and M. A. Garcia-Garibay, Ultrafast rotation in an amphidynamic crystalline metal organic framework, *Proc. Natl. Acad. Sci.*, 2017, **114**, 13613–13618.
35 J. T. Damron, J. Ma, R. Kurz, K. Saalwaechter, A. Matzger and A. Ramamoorthy, The Influence of Chemical Modification on Linker Rotational Dynamics in Metal Organic Frameworks, *Angew. Chem. Int. Ed.*., 2018, **57**, 8678–8681.
36 V. N. Vukotic, K. J. Harris, K. Zhu, R. W. Schurko and S. J. Loeb, Metal-organic frameworks with dynamic interlocked components, *Nat. Chem.*, 2012, **4**, 456–460.
37 K. Zhu, V. N. Vukotic, C. A. Okeefe, R. W. Schurko and S. J. Loeb, Metal-organic frameworks with mechanically interlocked pillars: Controlling ring dynamics in the solid-state via a reversible phase change, *J. Am. Chem. Soc.*, 2014, **136**, 7403–7409.
38 V. N. Vukotic, C. A. O. Keefe, K. Zhu, K. J. Harris, C. To, R. W. Schurko and S. J. Loeb, Mechanically Interlocked Linkers inside Metal − Organic Frameworks : Effect of Ring Size on Rotational Dynamics, *J. Am. Chem. Soc.*, 2015, **137**, 9643–9651.
39 K. Zhu, C. A. O'Keefe, V. N. Vukotic, R. W. Schurko and S. J. Loeb, A molecular shuttle that operates inside a metal-organic framework, *Nat. Chem.*, 2015, **7**, 514–519.
40 Q. Chen, J. Sun, P. Li, I. Hod, P. Z. Moghadam, Z. S. Kean, R. Q. Snurr, J. T. Hupp, O. K. Farha and J. F. Stoddart, A Redox-Active Bistable Molecular Switch Mounted inside a Metal-Organic Framework, *J. Am. Chem. Soc.*, 2016, **138**, 14242–14245.
41 M. Valášek, K. Edelmann, L. Gerhard, O. Fuhr, M. Lukas and M. Mayor, Synthesis of molecular tripods based on a rigid 9,9'-spirobifluorene scaffold, *J. Org. Chem.*, 2014, **79**, 7342–7357.
42 O. K. Farha, C. D. Malliakas, M. G. Kanatzidis and J. T. Hupp, Control over Catenation in Metal- Organic Frameworks via Rational Design of the Organic Building Block, *J. Am. Chem. Soc.*, 2010, **132**, 950–952.
43 S. T. Madrahimov, T. A. Atesin, O. Karagiaridi, A. A. Sarjeant, O. K. Farha, J. T. Hupp and S. T. Nguyen, Metal-organic frameworks containing (alkynyl)gold functionalities: A comparative evaluation of solvent-assisted linker exchange, de novo synthesis, and post-synthesis modification, *Cryst. Growth Des.*, 2014, **14**, 6320–6324.
44 O. Karagiaridi, W. Bury, J. E. Mondloch, J. T. Hupp and O. K. Farha, Solvent-assisted linker exchange: An alternative to the de novo synthesis of unattainable metal-organic frameworks, *Angew. Chem. Int. Ed.*, 2014, **53**, 4530–4540.
45 J. Conyard, K. Addison, I. A. Heisler, A. Cnossen, W. R. Browne, B. L. Feringa and S. R. Meech, Ultrafast dynamics in the power stroke of a molecular rotary motor, *Nat. Chem.*, 2012, **4**, 547–551.
46 A. P. Nelson, O. K. Farha, K. L. Mulfort and J. T. Hupp, Supercritical Processing as a Route to High Internal Surface Areas and Permanent Microporosity in Metal Organic Framework Materials, *J. Am. Chem. Soc.*, 2009, **131**, 458–460.
47 H. Huang, H. Sato and T. Aida, Crystalline Nanochannels with Pendant Azobenzene Groups: Steric or Polar Effects on Gas Adsorption and Diffusion?, *J. Am. Chem. Soc.*, 2017, **139**, 8784–8787.
48 J. W. Brown, B. L. Henderson, M. D. Kiesz, A. C. Whalley, W. Morris, S. Grunder, H. Deng, H. Furukawa, J. I. Zink, J. F. Stoddart and O. M. Yaghi, Photophysical pore control in an azobenzene-containing metal–organic framework, *Chem. Sci.*, 2013, **4**, 2858.
49 D. E. Williams, C. R. Martin, E. A. Dolgopolova, A. Swifton, D. C. Godfrey, O. A. Ejegbavwo, P. J. Pellechia, M. D. Smith and N. B. Shustova, Flipping the Switch: Fast Photoisomerization in a Confined Environment, *J. Am. Chem. Soc.*, 2018, **140**, 7611–7622.
50 B. J. Furlong and M. J. Katz, Bistable Dithienylethene-Based Metal-Organic Framework Illustrating Optically Induced Changes in Chemical Separations, *J. Am. Chem. Soc.*, 2017, **139**, 13280–13283.
51 C. L. Jones, A. J. Tansell and T. L. Easun, The lighter side of MOFs: structurally photoresponsive metal–organic frameworks, *J. Mater. Chem. A*, 2016, **4**, 6714–6723.
52 S. J. Tinnemans, M. H. F. Kox, M. W. Sletering, T. A. (Xander) Nijhuis, T. Visser and B. M. Weckhuysen, Dealing with a local heating effect when measuring catalytic solids in a reactor with Raman spectroscopy, *Phys. Chem. Chem. Phys.*, 2006, **8**, 2413.

53 P. J. Davis, L. Harris, A. Karim, A. L. Thompson, M. Gilpin, M. G. Moloney, M. J. Pound and C. Thompson, Substituted diaryldiazomethanes and diazofluorenes: Structure, reactivity and stability, *Tetrahedron Lett.*, 2011, **52**, 1553–1556.

54 C. Feldmeier, H. Bartling, E. Riedle and R. M. Gschwind, LED based NMR illumination device for mechanistic studies on photochemical reactions - Versatile and simple, yet surprisingly powerful, *J. Magn. Reson.*, 2013, **232**, 39–44.

55 M. A. . Frisch, M. J.; Trucks, G. W.; Schlegel, H. B.; Scuseria, G. E.; Robb, G. A. . N. Cheeseman, J. R.; Scalmani, G.; Barone, V.; Mennucci, B.; Petersson, G. . H.; Caricato, M.; Li, X.; Hratchian, H. P.; Izmaylov, A. F.; Bloino, J.; Zheng, J. . I. Sonnenberg, J. L.; Hada, M.; Ehara, M.; Toyota, K.; Fukuda, R.; Hasegawa, J. . M.; Nakajima, T.; Honda, Y.; Kitao, O.; Nakai, H.; Vreven, T.; Montgomery, J. A., K. N. . Peralta, J. E.; Ogliaro, F.; Bearpark, M.; Heyd, J. J.; Brothers, E.; Kudin, A. . B. Staroverov, V. N.; Kobayashi, R.; Normand, J.; Raghavachari, K.; Rendell, M. . K. J. C.; Iyengar, S. S.; Tomasi, J.; Cossi, M.; Rega, N.; Millam, N. J.; Klene, R. J. E.; Cross, J. B.; Bakken, V.; Adamo, C.; Jaramillo, J.; Gomperts, R.; Stratmann, R. L. . E.; Yazyev, O.; Austin, A. J.; Cammi, R.; Pomelli, C.; Ochterski, J. W.; Martin, J. J. . Morokuma, K.; Zakrzewski, V. G.; Voth, G. A.; Salvador, P.; Dannenberg, J. . Dapprich, S.; Daniels, A. D.; Farkas, Ö.; Foresman, J. B.; Ortiz, J. V.; Cioslowski and D. J. Fox, No Title, *Gaussian 09, Revis. D.01,*.

56 A. D. J. Becke, Density-functional thermochemistry. III. The role of exact exchange, *J. Chem. Phys.*, 1993, **98**, 5648–5652.

57 S. H. Vosko, L. Wilk and M. Nusair, Accurate spin-dependent electron liquid correlation energies for local spin density calculations: a critical analysis, *Can. J. Phys.*, 1980, **58**, 1200–1211.

58 C. Lee, W. Yang and R. G. Parr, Development of the Colle-Salvetti correlation-energy formula into a functional of the electron density, *Phys. Rev. B*, 1988, **37**, 785–789.